EVALUATION OF SPATIAL RESOLUTION AND LOCALIZATION ACCURACY OF ABSORBING HETEROGENITY EMBEDDED IN HOMOGENOUS AND LAYERED TURBID MEDIA USING FUNCTIONAL NEAR INFRARED SPECTROSCOPY

by

NIRANJANA NANDAKUMAR

Presented to the Faculty of the Graduate School of

The University of Texas at Arlington in Partial Fulfillment

of the Requirements

for the Degree of

MASTER OF SCIENCE IN BIOMEDICAL ENGINEERING

THE UNIVERSITY OF TEXAS AT ARLINGTON

August 2011

ACKNOWLEDGEMENTS

This thesis work would not have been possible without the guidance and support of several individuals who in one way or the other contributed their valuable time and assistance.

First and foremost, I would like to thank Dr.Georgios Alexandrakis for helping and guiding me in this research work by giving valuable suggestions and advice whenever needed. He was always patient and willing clear the questions that I had and guide me in the right track whenever needed.

I am grateful to Dr. Mario Romero-Ortega and Dr. Baohong Yuan for being my thesis committee members. They were very supportive and their precious suggestions paved way for the improvements in this thesis work.

I would like to show my gratitude to Bilal Khan for providing me with technical help and I am really happy about his willingness to assist me at anytime.

I would like to acknowledge my loving friends Raichel, Aswini, Sneha, Sonal, Karthik, Aishwarya and others who gave me strength and support.

I would like to thank my parents Nandakumar and Mohanavalli and my brother Sriram Prasad for their love and support. I am grateful to my aunt Sakunthala for her constant prayers and positive thoughts.

Finally, I am grateful to Almighty for providing me this life with all the essentials for existing and without whom I would not be what I am now at this moment.

July 14, 2011

ABSTRACT

EVALUATION OF SPATIAL RESOLUTION AND LOCALIZATION ACCURACY OF ABSORBING HETEROGENITY EMBEDDED IN HOMOGENOUS AND LAYERED TURBID MEDIA USING FUNCTIONAL NEAR INFRARED SPECTROSCOPY

Niranjana Nandakumar, M.S

The University of Texas at Arlington, 2011

Supervising Professor: Georgios Alexandrakis

Functional Near-Infrared Spectroscopy (fNIRS) is a non-invasive widely used technique for imaging the brain activation patterns in the cerebral cortex of neonates and adults. For the fNIRS imaging of these brain activation patterns, it is common to assume the head geometry as a homogenous medium due to the resulting computational simplicity of the image reconstruction problem. In reality the head is not a simple homogenous medium and prior research has been conducted to show that light propagates differently in a spatially heterogeneous model of the head compared to a homogenous one, which alters the sensitivity of NIR light detection on the head's surface. However, the effect of heterogeneous background tissue optical properties on the reconstructed fNIRS images has not been systematically studied to date. In this work, a planar layered media approximation of the head was employed as a first step towards modeling the effect of spatially heterogeneous tissues on the reconstructed fNIRS images. The effect of

neuronal activation on fNIRS measurements was simulated as in increase in absorption due to an increase in blood volume that occurred as a result of that activation. The increase in localized absorption relative to baseline values resulted in a decrease of measured NIR lightreflectance, as simulated by Monte Carlo. Subsequently, the diffusion approximation of NIR photon propagation in homogenous and layered was used in combination with a Tikhonov regularization procedure to reconstruct the simulated activation images. Spatial resolution, localization accuracy, and ovality metrics were quantified in the simulated fNIRS images. These virtual experiments were performed by placing a sub-resolution absorber of size 5 mm x 5 mm at three different locations within the field of view and by simulating fNIRS measurements for different source-detector geometries that ranged from sparse to very dense. Comparisons of reconstruction results and associated image metrics were performed between the layered head homogenous tissue models. It was found that the reconstructed images of the absorber for the homogenous and the layered medium were qualitatively similar. In addition, as it is not possible to know the exact optical properties of the brain tissues of each subject being imaged, the changes in spatial resolution and localization accuracy were assessed for variations in the background tissue transport scattering coefficient (μ_s') by ±50% and ±25%. The results showed that both the homogenous and the layered geometry are insensitive to incorrect knowledge of the background μ_s' values. It is concluded that spatial resolution and localization accuracy largely depend on the source-detector geometry when reconstructing fNIRS images in planar, laterally infinite, geometry tissues.

TABLE OF CONTENTS

LIST OF ILLUSTRATIONS

Figure

LIST OF TABLES

CHAPTER 1

INTRODUCTION

1.1 Functional Near Infrared Spectroscopy

Functional brain imaging or functional neuroimaging involves non-invasive or minimally invasive techniques that investigate the cerebral functions and metabolism. Earlier, it was common to use Electroencephalography (EEG) for mapping of electrical signals that corresponds to the neuronal activities in the brain [1]. Advancement in the field has lead from mapping of neuronal signals to imaging of the structural and functional changes in the brain. Increase in metabolic activity in a brain area causes an increase in the local blood flow by neurovascular coupling. This increased blood flow causes an increase in local concentration of oxy- hemoglobin (HbO_2) and a decrease in the concentration of the deoxy-hemoglobin (HbR).The hemodynamic response due to neuronal activation can be imaged by using functional magnetic resonance imaging (fMRI), positron emission tomography (PET), single photon emission tomography (SPECT), and near-infrared spectroscopy (NIRS) [2].Functional Near-Infrared Spectroscopy (fNIRS) technique enables imaging of cortical activation patterns and offers the advantage of being portable, which enables longitudinal sides in the doctor's office or by the hospital bedside. As a result, fNIRS has been widely used for studying the neurobehavioral developments in infants and young children [3, 4] and functional reorganization during rehabilitation from stroke, among other applications [5, 6]. This technique has a spatial resolution of about 1 cm [5] and a good temporal resolution of hundreds of ms [7].

1.1.1 Near-Infrared Imaging Principle

The NIR photons have a wavelength range of 650-950nm in the electromagnetic spectrum. The light in this 'optical window' is weakly absorbed by the tissue and hence this

property allows light to penetrate several centimeters through the tissue [1].The two dominant chromophores in the NIR range are HbR and HbO_2 [8].

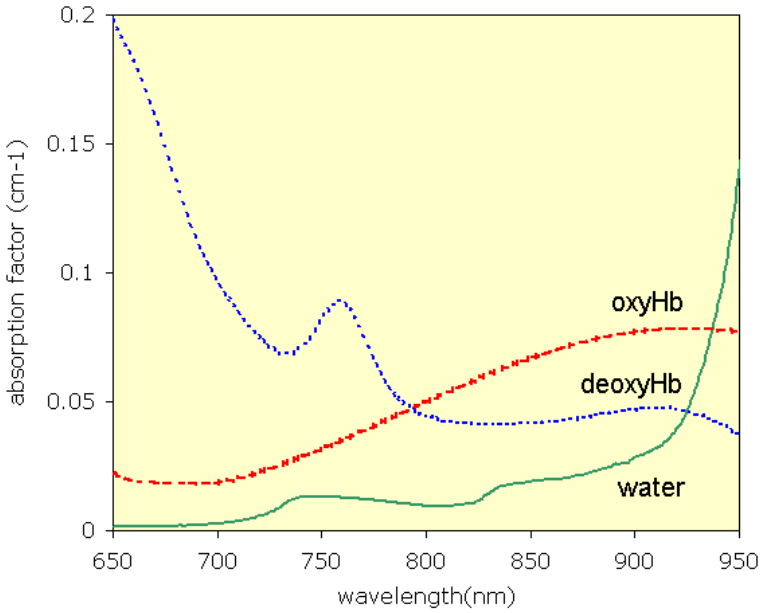

Figure 1.1 Absorption Spectra for Oxy and Deoxy Hemoglobin [10]

At shorter wavelengths in this optical window, the absorption of light by HbO_2 is dominant whereas at longer wavelengths, absorption from HbR is higher. These differences in the absorption spectra of HbR and HbO_2 allow the separate measurement of concentrations of these two species[7].These concentration measurements provide information on blood volume and oxygenation[7, 8].Separation of the contributions from these two hemoglobin species is attained by performing measurements at wavelengths on either side of 800 nm (the isosbestic point of hemoglobin) [8].

The interaction of light with biological tissues is described by the absorption coefficient (μ_a) and the scattering coefficient (μ_s).It is the inverse of the mean distance travelled between absorption/scattering events and they are measured in mm^{-1}. As the tissue's scattering coefficient is typically much larger than absorption, scattering dominates light transport and

hence the back-reflected light, even only a few millimeters away from the light source, is highly diffused as shown in figure 1.2.

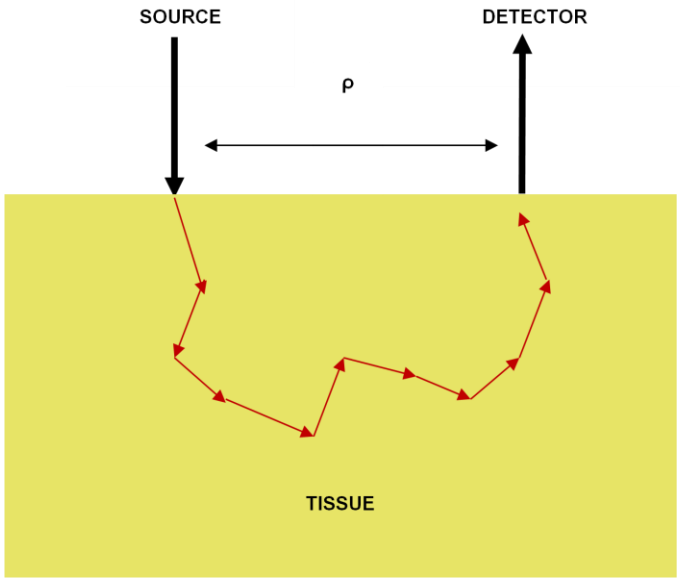

Figure 1.2 Multiple Scattering of NIR Photons in Turbid Tissue Media

The mean pathlength travelled and the mean depth visited by NIR light in tissue both increase for photons existing tissue at larger distances from the light source [1, 9].Therefore by placing detectors at different distances from the source helps to gain some control over the tissue depth that can be probed. The sensitivity region inside the tissue for each source-detector (S-D) pair is banana-shaped [1, 5] and the depth of maximum sensitivity is approximately half the distance of the S-D separation [1].

In Figure 1.3, for an S-D separation of 3 cm, the maximum sensitivity region is approximately at 1.5 cm below the surface of the scalp which centers the banana-shaped sensitivity function approximately at the depth of the cortical grey matter. When performing fNIRS, images are typically reconstructed on the plane of the cortex and it is assumed that the increase in local blood volume and oxygenation, secondary to neuronal activation, change only the absorption coefficient and not the scattering coefficient of cortical tissue while the scalp and skull contribute little or no change to these measurements[1].

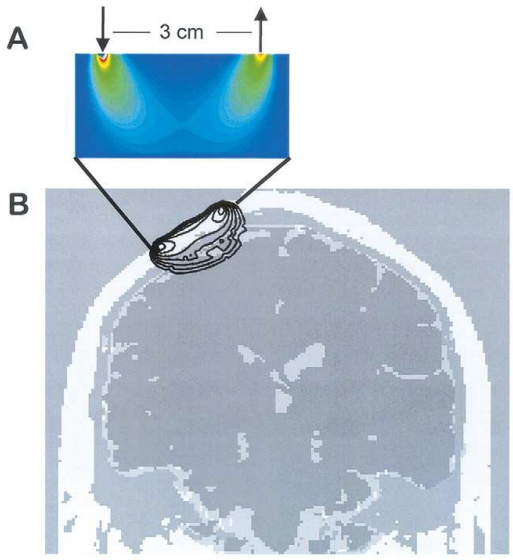

Figure 1.3 (a) An example of sensitivity plot for light traveling in a homogenous, highly scattering medium for an S-D separation of 3 cm and (b) A plot for light traveling through the head of an example subject [1]

The fNIR imaging method employs the overlapping measurements of interlaced source-detector pairs such that each detector receives light from multiple sources. The light detected is further processed to produce spatially resolved images as is described below. The images obtained are maps of changes in HbR and HbO2 that can be recalculated as images of changes in oxygen saturation [8].

1.1.2 Modified Beer-Lambert's law

The fNIRS method uses the modified Beer-Lambert law (MBLL) to quantify changes in the concentration of hemoglobin, the biological chromophore [6].This law is an empirical description of optical attenuation in a highly scattering medium.

Equation (1.1) explains the MBLL:

$$OD=-\log\left(\frac{I}{I_o}\right)= \varepsilon CLB+G \qquad (1.1)$$

Where OD is optical density, I and I_0 are the detected and incident light intensities respectively, ε is the extinction coefficient of the chromophore, C is the concentration of the chromophore, L is the distance between the source and the detector, B is the pathlength factor caused by tissue scattering and G is a factor that accounts for the measurement geometry.

A change in the concentration of an absorbing species causes a change in the detected light intensity and the concentration change is proportional to the logarithm of the ratio of light intensity before and after the change [6, 7]:

$$\Delta OD=-\log\left(\frac{I}{Io}\right)=\varepsilon\Delta CLB \quad (1.2)$$

where ΔOD is the change in the optical density and ΔC is the change in the concentration.

The contribution to the total change in optical density from both chromophores is then calculated as:

$$\Delta OD^{\lambda}=(\varepsilon^{\lambda}_{HbO}\Delta[HbO] + \varepsilon^{\lambda}_{HbR}\Delta[HbR])B^{\lambda}L \quad (1.3)$$

where $[HbO_2]$ and [HbR] are the concentrations of HbO_2 and HbR respectively, ε is the extinction co-efficient and λ is the measurement at a particular wavelength.

The concentration changes of the two chromophores can be determined by taking measurements at two different wavelengths and using the extinction coefficients of the two chromophores at those wavelengths. Researchers have proved that pairing 660-760 nm with 830 nm provide very good separation of HbR and HbO_2 while noise performance is good at 870nm or 890nm [9, 10].Another research concluded that the potential for cross- talk was reduced 10 times when using a wavelength pair of 690 and 830nm than when using 780 and 830 nm [10].Thus, it is very important to carefully consider the optimum wavelength pair while estimating the hemoglobin concentration.

1.1.3 Radiative transport equation for photon migration

The radiative transport equation (RTE) describes light propagation in turbid media. It is a very accurate model but is difficult to solve without introducing approximations[13].The diffusion equation, which is an approximation to the RTE, is written as

$$\nabla.D(r)\nabla\Phi(r,t)-v\mu_a(r)\varphi(r,t)+vS(r,t)=\frac{\partial\Phi(r,t)}{\partial t} \quad (1.4)$$

where$\Phi(r,t)$ is the photon fluence at position r and time t.S(r,t)is the source distribution of photons.$D=v/(3\mu_s')$ is the diffusion coefficient, μ_s' is the reduced scattering coefficient with $\mu_s'=(1-g)\,\mu_s$, $\mu_a$is the absorption coefficient, and v is the speed of light in the medium.

For the combination of the two hemoglobin chromophores, μ_a is calculated as:

$$\mu_a=\varepsilon_{HbO}[HbO]+\varepsilon_{Hb}[Hb] \quad (1.5)$$

and the above equation is wavelength dependent.

Solutions to the photon diffusion equation can be obtained either stochastically (Monte Carlo method, Markov random field method, or Random walk theory) or deterministically (Analytical method, Finite- difference or Finite-element methods) [14].

1.1.4 Solution to the Diffusion Equation

For a turbid medium in a spatially homogeneous semi-infinite geometry the photon diffusion equation can be solved analytically by applying the extrapolated boundary condition and Green's function solution for an isotropic point source located at 1 mean free path from the medium's surface [15-19].In the extrapolated boundary condition, a point light source is placed at a distance z_0 inside the tissue and a virtual negative light source is placed at $-z_0$ (outside the tissue medium) to set the fluence of photons at an extrapolated boundary z_b (between z_0 and $-z_0$) to zero. The Green's function solution considers the source as a delta function, i.e. all photons have scattered isotropically at a single mean free path, for solving the diffusion equation with the above stated boundary conditions.

The solution of the diffusion equation for a CW source [20] is,

$$\Phi(r_s,r_d)=\frac{vS}{4\Pi D}\left[\frac{\exp\left(-\sqrt{3\mu_s'\mu_a}|r_s-r_d|\right)}{|r_s-r_d|}-\frac{\exp\left(-\sqrt{3\mu_s'\mu_a}|r_{s,i}-r_d|\right)}{|r_{s,i}-r_d|}\right] \quad (1.6)$$

where $\Phi(r_s,r_d)$ is the photon fluence at a detector position r_d due to the point source r_s.$D=v/(3\mu_s')$ is the photon diffusion coefficient, $r_{s,i}$is the image source.

Two standard approaches to find linear solutions when the μa is spatially varying are the Born andRytov approximations [22].In this work, we used Homer software [17] that used rytov approximation.

The Rytov approximation is defined as:

$$\Phi = \Phi_o \exp(\Phi_{pert}) \quad (1.7)$$

where the total fluence Φ is decomposed into Φ_0 which only depends on the background optical properties μ_{ao} and μ_{so}', and Φ_{pert}which is linearly related to spatial variations in $\Delta\mu_a$:

$$\Phi_{pert}(r_s,r_d) = -\frac{1}{\Phi o(r_s,r_d)} \int \Phi o(r_s,r) \frac{v\Delta\mu_a(r)}{D_o} G(r,r_d)dr \quad (1.8)$$

wherer_s and r_d are the positions of the source and detectors respectively, G is the Green's function of the photon diffusion equation for the background optical properties given the boundary conditions.

The above equation can be written in matrix form by rewriting the integral as a sum over the voxels:

$$\mathbf{y} = A\mathbf{x} \quad (1.9)$$

where y is the vector of measurements $\Phi_{pert}(r_s,r_d)$, x is the vector of image voxels $\Delta\mu_a(r)$, A is the sensitivity matrix obtained from the integrand of equation 1.8 [6].

The homogenous medium is only an approximate model of the head geometry and in this work it was hypothesized that modeling the heterogeneous background optical properties more accurately could potentially improve the localization of activation regions. As a first approximation to the rather complex head geometry the scalp, skull, cerebrospinal fluid (CSF) and grey matter were modeled as semi-infinite planar layers.

The diffusion equation of light in the layered medium was solved by numerical method using the Fourier transform approach and extrapolated boundary condition [19].

Applying the Fourier transform to the diffusion equation:

$$\frac{\partial}{\partial z^2}\Phi_1(z,s) - \alpha_1\Phi_1(z,s) = -\frac{1}{D_1}\delta(z-z_0), \qquad 0 \le z < l_1 \quad (1.10)$$

$$\frac{\partial}{\partial z^2}\Phi_k(z,s) - \alpha^2{}_k\Phi_k(z,s) = 0, \quad \sum_{j=1}^{k-1} l_j < z \le \sum_{j=1}^{k-1} l_j, \qquad k=2,3,\ldots,N \quad (1.11)$$

Where l_k is the thickness of layer k, Φ_k is the fluence rate, $D_k=1/[3(\mu_{sk}'+\mu_{ak})]$ is the diffusion coefficient, $s=(s_1^2+s_2^2)^{1/2}$ and $\alpha_k^2=(D_k s^2+\mu_{ak})/D_k$. The diffusion equation was solved for the

extrapolated boundary condition and the inverse Fourier transform was applied to the solution obtained in Fourier space.

1.1.5 The Monte Carlo Method

One possible way of validating the approximate solutions to the RTE is to simulate the fNIRS imaging process by Monte Carlo, which is a stochastic method that models the individual photon trajectories [23].This is the most commonly used stochastic simulation method in the NIR imaging field and is often regarded as the 'gold standard' [8].Photon propagation in the tissue model is as follows:

1. Initial position and the direction of the photon are defined in the configuration file.

2. After a photon is launched, it is moved to a distance of Δs which where it can be scattered, absorbed, propagated undisturbed, internally reflected, or transmitted out of the tissue.

$\Delta s << 1/\mu_t = 1/ (\mu_s+\mu_a)$

μ_t, μ_s and μ_a are total attenuation, scattering and absorption coefficients respectively.

3. Photon is moved to the next scattering event after reflecting or refracting at interfaces. As the photon is moved from voxel to voxel, it gets attenuated based on the local absorption and the distance travelled in each tissue type is recorded.

4. As the photon moves, its position is sampled at regular time intervals and this is used to update the accumulated photon density in each voxel of the simulated tissue volume.

5. The photon is scattered into a new direction according to some (possibly isotropic) phase function

6. Iteration is done until the photon leaves the system, or the time limit is exceeded.

7. If the photon exists within the geometrical bounds of a detector, the path length it has spent in each distinct tissue type is recorded in a history file before the simulation of the trajectory for the next photon begins.

Monte Carlo can be used for computing both the change in reflectance due to the presence of an absorber (ΔOD) as well as the A-matrix. In this research work, simulation was

done to obtain only ΔOD whereas the A-matrix was computed as described in the Methods section.

1.3 Prior Work

Most fNIRS studies to date have considered the head as a homogeneous medium as far as the sensitivity matrix calculation is concerned [17] due to the computational expediency of the analytical solution to the diffusion equation for this tissue geometry. Using this simplifying assumption prior work has been performed to test the localization accuracy and resolution in homogeneous media [17].

A few studies have been published on studying light propagation in layered media approximating the brain geometry, which indicated that light propagation is affected by the presence of a low-scattering CSF layer and the sensitivity of the absorption change in gray matter is improved [24-26].However, no study has been performed to date to assess the effect of these differences between the A-matrix of semi-infinite versus layered media on the resulting reconstructed images. This is also true for other published work where light migration through the head was modeled based on an MRI model with the different segmented tissues being assigned optical properties appropriate for each tissue type [20, 24, 25, 26].Simulations of photon propagation and sensitivity analysis in the MRI-based head geometry have been performed by Monte Carlo [24-26].However, reconstructed images from simulations in such geometries have not yet been reported, possibly due to the noise involved in the stochastic estimation of the A-matrix by this method.

1.4 Objective of Study

Previous studies of NIR photon propagation through a layered medium model of the head have examined the changes in reflectance profiles that result from assuming such a tissue geometry relative to a homogeneous one [24- 26]. However, there has been no study to date focusing on how the assumption of layered tissue geometry affects the spatial resolution of reconstructed images in fNIRS. This work focuses on answering this question, i.e. what is the

spatial resolution of fNIRS in layered media compared to homogeneous media for the same absorber location and source-detector geometry. These comparisons are performed for rather sparse up to very dense source-detector geometries. Also, since it is not possible to know the actual background optical properties of each human subject's head the effect of wrongly assumed background optical properties on the spatial resolution of reconstructed images is also studied. More specifically, this study examined the following three specific hypotheses:

Hypothesis 1:

Spatial resolution and localization for isolated absorbers improves when using a layered media model for the head tissues versus using a homogenous media model.

Hypothesis 2:

Spatial resolution and localization for isolated absorbers improves when increasing source-detector density both for layered and homogeneous models of the head tissues.

Hypothesis 3:

Changes in the assumed background tissue μ_s' values affect the spatial resolution and localization accuracy of isolated absorbers both for layered and homogenous media geometries.

CHAPTER 2

MATERIALS AND METHODS

2.1 Optical Imaging Systems for fNIRS

For most fNIRS brain imaging studies, continuous wave (CW) systems are being used because of the higher temporal resolution that can be achieved at a good signal-to-noise and the substantially lower cost of light sources and photon detectors compared to time-resolved systems [8]. Recently, time domain (TD) systems using picosecond duration pulses, have been shown to achieve good depth resolution due to their time-gating capacity relative to CW systems, but such systems have yet to attain the commercial markets mainly due to the aforementioned cost issues [8] [15].In this thesis work the S-D geometries simulated were those previously employed in conjunction with commercially available CW imagers, namely the CW-5 (TechenInc, Milford, MA) and DYNOT (dynamic near- infrared optical tomography, NIRx Medical technologies, NY)

DYNOT uses a time-division multiplexed illumination technique to perform measurements from multiple S-D pairs at sampling rates of up to 10 Hz while performing measurements at two wavelengths, 760nm and 830 nm, simultaneously by frequency encoding.CW-5 also performs two-wavelength measurements, 690 nm and 830 nm, with sampling rates up to 100 Hz, and uses frequency-division multiplexed sources.

In this study, no physical measurements were performed, but only the image formation process was simulated. The idealized systems were simulated with no time dependant hemodynamic fluctuations of the activation region, nor additional fluctuations originating from the scalp. The latter are typically measured experimentally at short source-detector separations and then adaptively filtered out of the signals from larger separations [5-6].Instead there were only two snap-shots in time for each measurement – one simulation with the absorber in place

(activation) and one without (no activation). Given the static nature of these simulations, only the effect of S-D geometry used in prior work [28-31], was investigated for its effect on spatial resolution in fNIRS.

Simulations for both spatially homogeneous and layered media were performed using the optical properties described below. In the actual experimental setting, the measurements of light intensity was done at baseline when the person was not performing any task and during activation state where the person performed some task, say finger tapping for 10-15 seconds. In this research work, the activation was simulated by a static absorber and the ΔOD for the equation y=Ax was simulated by Monte Carlo. This helped to easily embed the absorber anywhere within the field of view (FOV) and study the effects of the placement of the absorber with respect to the optode geometry. The A-matrix was calculated using the semi-infinite and layered approximations to the diffusion equations because computationally less expensive solutions exist for these tissue geometries [15-19].

2.2 Optical Properties of the Tissues for the Simulations

The human brain is a very complex structure and is the center of human nervous system. It is protected and surrounded by the skin, the skull, the meninges (dura mater, arachnoid mater and the pia mater), and the watery cerebrospinal fluid (CSF). In this research work, only the four layers that play a major role in NIR light propagation are considered. These are the scalp, the skull, the CSF and the gray matter. Modeling the white matter was not important for this work because very little light reaches that depth for the source-detector geometries used. The thinner dura mater layer was lumped together with the skull and the pia and arachnoid mater were ignored because they are very thin [22]

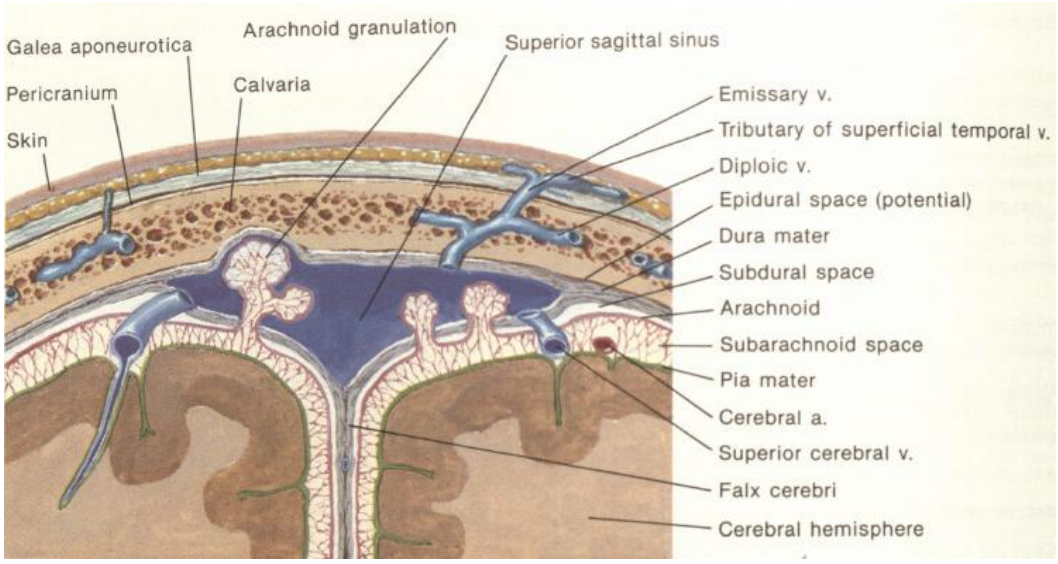

Figure 2.1 Human Brain and Its Layers [23]

For the spatial resolution and localization studies performed in this work two types of media were considered in the simulations: i) a homogenous medium and ii) a layered medium.

Figure 2.1 shows the layers considered for simulation in the layered model of the head. The homogenous, semi- infinite model optical properties represent a value that was representative of an average value for these tissue layers [5] [17] with, μ_s'=1.1 mm^{-1} and μ_a= 0.0186 mm^{-1} being assumed for this simulation work. For the layered head geometry, the table 2.1 shows the tissue optical properties in each layer at a wavelength of 830nm where HbO_2 is the dominant chromophore. μ_s' of CSF was used for MC calculation but not for solving the diffusion equation due to the instability of the solver. Hence, μ_s' of the skull was used in the place of μ_s' of CSF only for solving the diffusion equation.

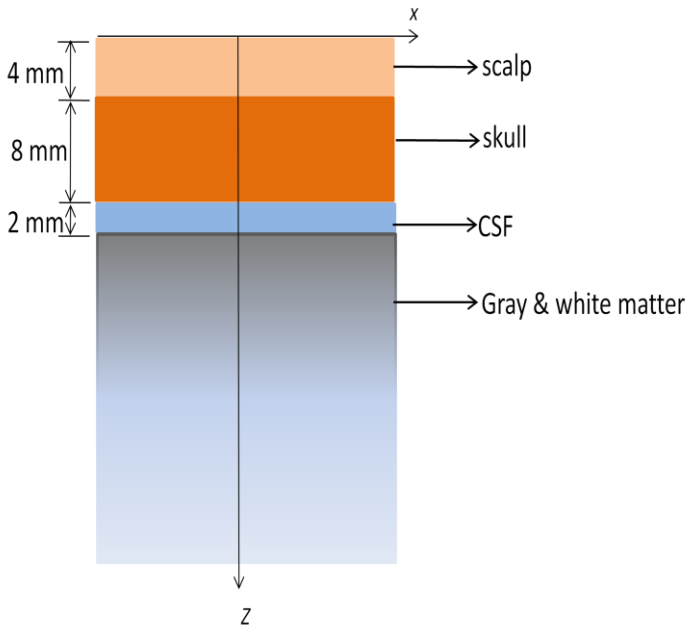

Figure 2.2 Layered Medium Used for the Forward Model

Table 2.1 Optical Absorption and Scattering Properties at 830nm Used in the Calculation of Tissue reflectance [31]

Tissue type	**Thickness (mm)**	**μ_a mm-1**	**μ_s' mm-1**
Scalp	4	0.0191	0.66
Skull	8	0.0136	0.86
CSF	2	0.0026	0.01
Gray matter+ white matter	Semi- infinite	0.0186	1.11

As it is not possible to know precisely the optical properties of the head of each patient, imaging simulations were performed while assuming wrong optical properties for the reflectance computation model. Specifically the μ_s' of the scattering medium was perturbed by ±25% and ±50% in both the layered and semi-infinite tissue media.

2.3 Monte Carlo simulations for reflectance measurements

tMCimg was the software used to perform a Monte Carlo simulations of photon transport through 3D volumes with spatially varying optical properties and arbitrary boundary conditions [18]. It supports both the highly scattering and weakly scattering tissue types.

The output of the simulation yielded two data files: i) history files ii) two-point files. The history file was used for the reflectance measurement and it contained the information on the number of the detector that recorded the photon and the pathlength inside each of the n tissue for all exiting photons. Following is the format of the history file:

$d_1\ t_1\ l_1^{(0)}\ l_1^{(1)}\ \dots\ l_1^{(n)}$

$d_2\ \ t_2\ l_2^{(0)}\ l_2^{(1)}\ \dots\ l_2^{(n)}$

.
.
.

$d_n t_n\ l_n^{(0)}\ l_n^{(1)}\ \dots\ l_n^{(n)}$

All the simulations were done using 10^8 photons. ΔOD in MBLL is the negative logarithm of the ratio of the fluence in the presence of the absorber to the fluence without the absorber. MATLAB was used for fluence calculation from the history file of the simulation.Since the optical properties of that of the absorber were set to the same as that of the background during the simulation, it has reduced the computational time of simulation for calculating the fluence with and without the absorber separately. Thus, history file was processed twice, once with the absorber in place and once without and then the logarithm of the ratio was computed to give the ΔOD which corresponded to 'y' in y=Ax (equation 1.9)

2.4 Probe Geometries

Four probe geometries were considered in this work: a sparse CW5 system geometry (Figure 2.3 a) and three DYNOT system geometries of different source-detector grid densities with SD pair distances of 2.2cm, 1.1cm and 0.75 cm (Figure 2.3 b-d).In the CW-5 system simulations sources (x's in Figure 2.3 a) and detectors (o's in Figure 2.3 a) where physically

separate whereas in the DYNOT system simulations these co-localized as this system uses bifurcated fiber bundles to deliver and collect light from the scalp. Details of these source-detector geometries were as follows:

Geometry1 (G-1, Figure 2.3 a): This was CW-5 geometry with SD spacing of 3.1 cm and source-detector separation of 2 cm. The FOV size was 6 cm x 6 cm and the number of measurements were12 given that SD pairs at distances greater than 3.1 cm had very low signal.

Geometry2 (G-2, Figure 2.3 b): This was grid geometry with an inter-optode distance of 2.2 cm.The FOV for this geometry was 4.4 cm x 4.4 cm and the number of measurements was 40 after including nearest neighbor and next-nearest neighbor measurements at source-detector separations of 2.2 cm and 3.1 cm respectively.

Geometry3 (G-3, Figure 2.3 c): The inter-optode distance was decreased from the previous geometry to 1.1 cm. The FOV size remained the same at 4.4 cm x 4.4 cm but the number of measurements increased to 336 as all detectors within 3.1 cm of each source were included.

Geometry4 (G-4, Figure 2.3 d): The inter-optode distance for this geometry was 0.75 cm and the FOV was 4.5 cm x 4.5 cm. The number of measurements was 1170 after including all but the 0.75 cm separation detectors within a distance of 3 cm form each source. The short-distance measurements were excluded because they did not probe the absorber depth while contributing significant Monte Carlo generated stochastic noise to the simulated measurements.

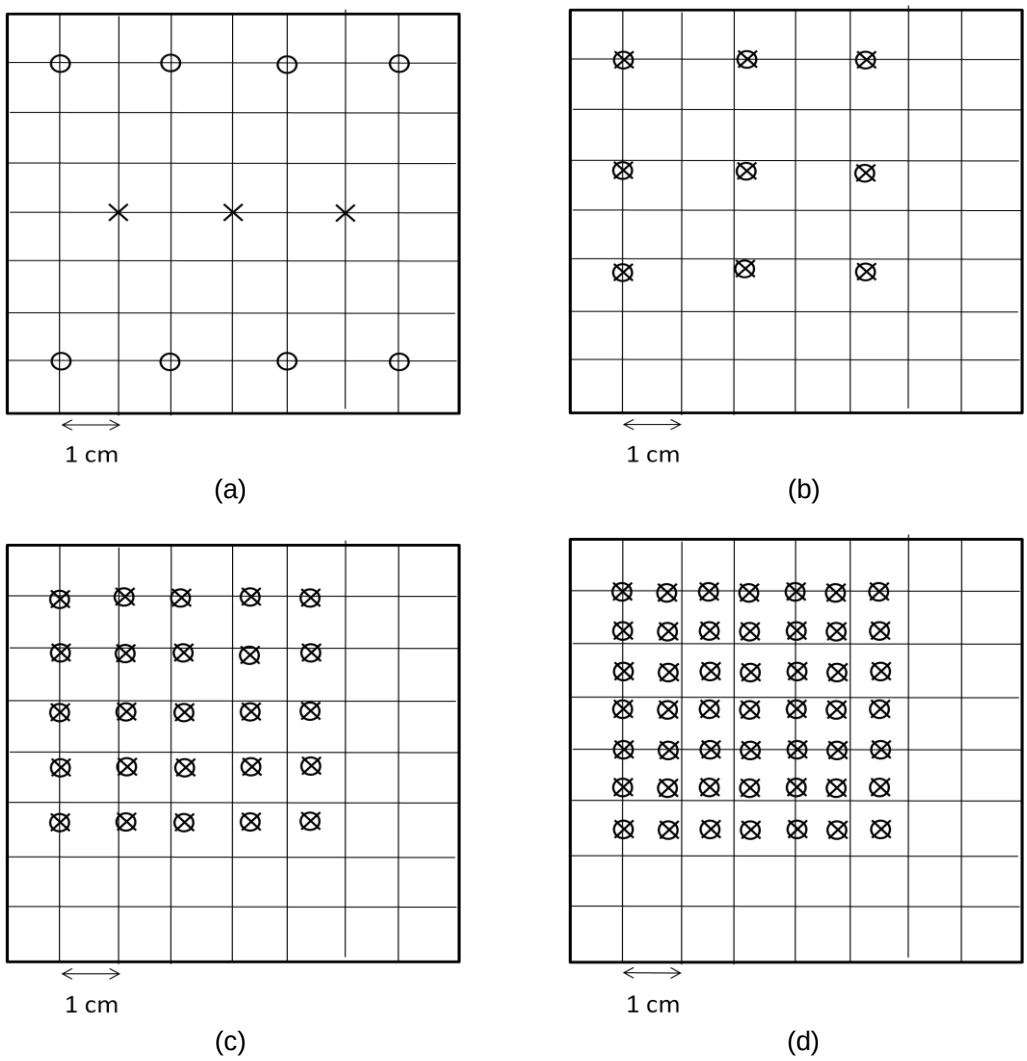

Figure 2.3 Probe geometries used for the simulation. (a) G1- CW5 (b) G2- DYNOT (2.2cm). (c) G3- DYNOT (1.1 cm) (d) G4- DYNOT (0.75 cm).
In these panels x's are sources and o's are detector

2.5 Absorber locations

In this work, three absorber positions were considered: i) At one corner of the FOV and below a detector, ii) At the center of the FOV and directly below a detector position, and iii) at the most sensitive position for detection (diagonally between S-D pairs near the center of the FOV).The size of the simulated square absorber was 5 mm x 5 mm and was placed at a depth of 15 mm, simulating the existence of hemodynamic activation in gray matter. The size of the

absorber was decided such that it would be smaller than the typical known resolution limit of ~1 cm for fNIRS in semi-infinite media, but large enough to give measurable signal change in the Monte Carlo data. The μ_a of the absorber used was 0.000974 mm^{-1} higher than the baseline μ_a and was calculated with $\Delta C=10^{-5}$ M ($[HbO_2]$ – [HbR]) and ε_{HbO2} = 974 cm^{-1}/M at 830 nm [21].

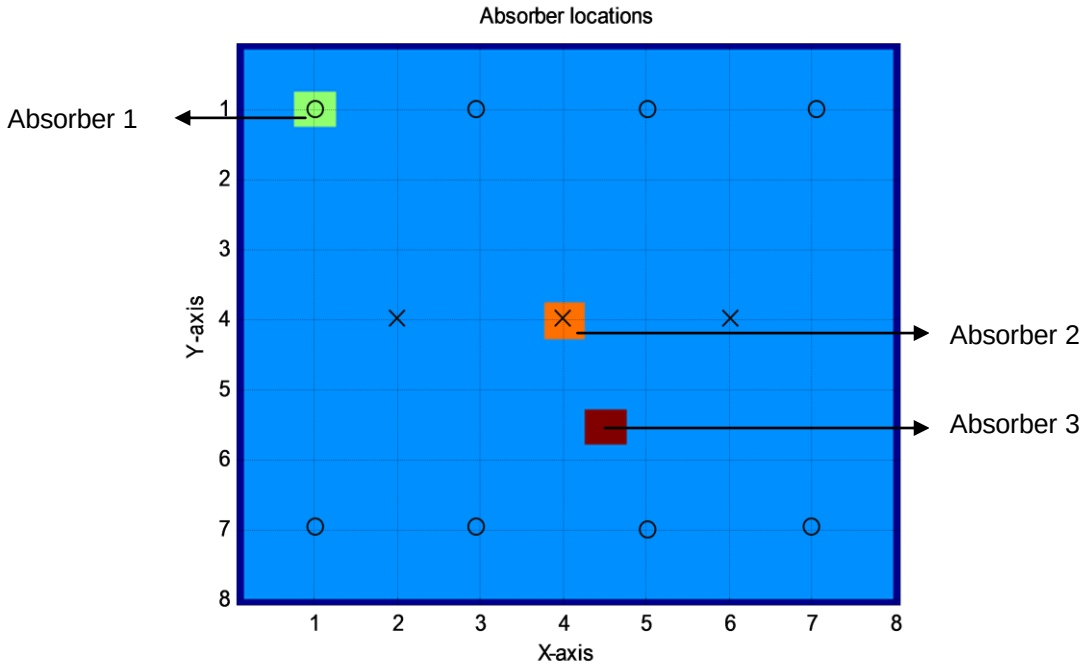

Figure 2.4 Absorber Locations Shown for the CW-5 Geometry

2.6 Computation of the Sensitivity Matrix and Image Reconstruction

The sensitivity matrix (A matrix) was computed using the forward solution to the diffuse photon propagation models for both the homogenous and the layered media. More specifically, the Greens function solution was first computed from source to points in the FOV where the absorber was placed. The Greens function solution represented the probability of the number of photons reaching a particular point considered in the medium and the probability that a photon originating from that location will reach a given detector. Due to principle of reversibility of light, the probability of photons from the medium to the detector is calculated as the probability of photon from the detector that reached the medium. These two probabilities are then multiplied

to each other for each pixel location in the FOV for a given S-D pair, thus defining a row of A-matrix (sensitivity matrix).

The analytical Green's function solution to the diffusion solution for a homogenous medium [17] was implemented in MATLAB. It was calculated for the background optical properties and an extrapolated boundary condition. For the layered medium, a light diffusion solver in the steady state domain [19] by AlwinKienle was used for the same calculations as described above for the semi-infinite medium. For both geometries, after the two-point Greens function solutions were calculated, these were multiplied together to get the A-matrix entry in that particular voxel for the S-D pair considered, as explained above. This calculation was repeated for all the S-D pairs and the FOV considered for the A-matrix. Thus, the A-matrix is composed of the rows of all source-detector pairs stacked one below the other. Image reconstruction was done in MATLAB using the Tikhonov regularized inversion [17] with a regularization parameter of $\alpha = 0.5$.

2.7 Evaluation of Spatial Resolution

Four parameters were used for studying the spatial resolution in the reconstructed images:

1. Area ratio (AR): The reconstructed image of an absorber is often distorted or blurred due to the diffuse nature of the light. The area of the absorber in the reconstructed image was computed by counting all the pixels that are above a threshold value. The threshold value is the maximum value of the noise in the image and was computed after applying the k-means clustering algorithm which arranges each of the image pixels into one of the 3 clusters: activation, deactivation and noise. AR was defined as

$$AR=\frac{Ar}{Ao}$$

where Ar was the area of the reconstructed absorber and Ao the true area of the absorber

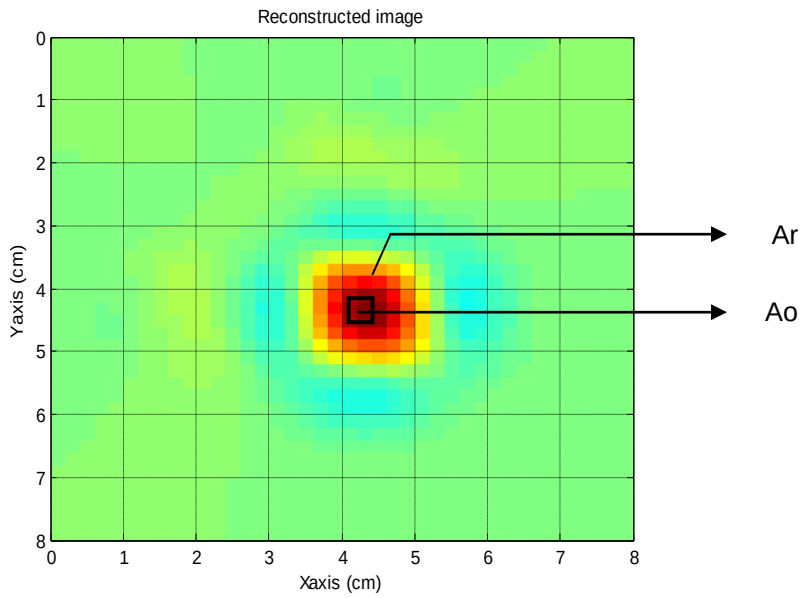

Figure 2.5 Actual Absorber (Black- Edged Square) Superimposed on the Reconstructed Image. Ar=Area of the reconstructed absorber, Ao= Area of actual absorber

2. Localization error (LE): To determine the accuracy of localization of the center of mass of the absorber in the reconstructed image, the shift in the center of the reconstructed absorber with respect to the known center of the absorber was computed as:

$$LE=\sqrt{(x-xo)^2+(y-yo)^2}$$

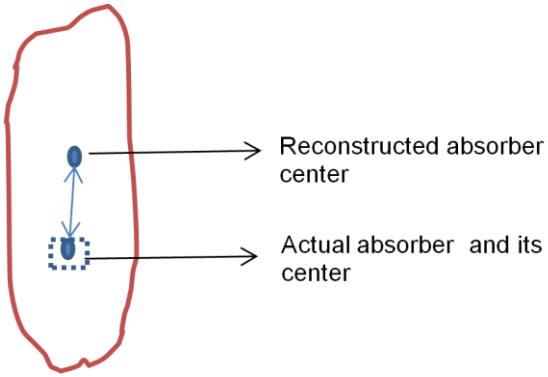

Figure 2.6 An Example to Show Localization Error (LE). The red outline indicates the reconstructed absorber while the dotted square indicates the actual absorber.The double-headed arrow shows the LE

The center of the reconstructed absorber was computed from the threshold image using the following formulae:

Center of mass (x) = $\frac{m1x1+m2x2+\ldots+mnxn}{m1+m2+\ldots+mn}$, Center of mass (y) = $\frac{m1y1+m2y2+\ldots+mnyn}{m1+m2+\ldots+mn}$

where m= image pixel value and x,y= co-ordinate of the pixel.

3.Full width at half maximum (FWHM): This was the maximum of the major or minor axis value which was obtained from the two-dimensional fit performed for the Ovality calculation as described below.

FWHM≈2.35482 σ

4. Ovality: This was used as a measure of the deviation of the reconstructed absorber's shape from circularity. In the reconstructed image, the absorber shape is influenced by the SD separations and directions and often appears to be elongated in some preferential direction that is typically along diagonals connecting source-detector pairs. A two-dimensional Gaussian fit for the reconstructed absorber was performed to obtain the Full Width Half Maximum (FWHM) of the major axis (a) and minor axis (b) of the absorber, which was then used for the ovality measurement.

Ovality=$\frac{2(a-b)}{(a+b)}$

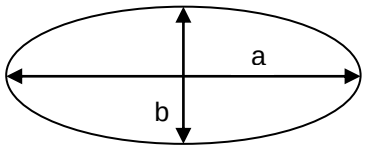

Figure 2.7 Example to Show Ovality

The error for each the above image metrics can be estimated by repeating the Monte Carlo simulations using a different seed number and processing the resulting reconstructed images as outlined above. Though no physical experiments were performed in this work, in a real world scenario, estimates for these metrics could be attained from repeat measurements on the same subjects, or by analyzing individual rest-activation intervals and subsequently computing mean and standard deviation values.

CHAPTER 3

RESULTS AND DISCUSSION

Cortical activation was simulated using the tMCimg Monte Carlo code [20] as an absorber of 5 x 5 mm size placed at three different locations in the FOV and for four different source-detector geometries, as described in the Methods Section above. The change in reflectance for each source-detector pair due to activation was simulated for both the homogenous and layered media for the baseline tissue optical properties listed in the Methods Section. This Section describes how the resulting reconstructed images differ, based on a series of quantitative metrics, for each activation location depending on the source-detector arrangement and background optical property model used. Changes in corresponding reconstructed results when assuming false background optical properties are also discussed.

3.1 Comparison of Image Metrics for a Homogenous and a Layered Medium Tissue Geometry for Different Absorber Locations and Optode Geometries

3.1.1 Anomaly 1

The reconstructed images of Anomaly 1 (black-edged square located below a detector at the top-left corner of the FOV in Figs 3.1 and 3.2) for different optode geometries were compared for the homogenous and layered medium tissues.

Figure 3.1 shows the reconstructed images for the homogenous medium and Fig. 3.2 corresponding results for the layered medium, respectively. In the case of G1, the absorber is projected along the diagonal linking the nearest S-D pair. For the grid S-D geometries, G2 through G4, the absorber is more localized near its true location though the spatial extent of the activation in the reconstructed image is much larger than its true size. However, the size of activation decreased with increasing S-D density up to a spacing of 1.1 cm. For the highest

S-D density of 0.75 mm the size of the activation did not shrink and it in fact grew a little larger, possibly due to the extra noise coming from the Monte Carlo simulated data for S-D pairs that do not sample the activation region. Corresponding results for the layered tissue geometry, shown in Fig. 3.2, show qualitatively similar trends for the reconstructed images. Changes in spatial resolution, defined as the ratio of activation area in the image versus the true area of the absorber, as a function of S-D geometry for the two tissue geometries is shown in Fig. 3.3a. It was seen that spatial resolution increases from G1 to G3 for both the types of medium. This is due to the increase of overlapping S-D pairs sampling the absorber location. In case of G4, the spatial resolution of the absorber degrades from the previous geometry due to the presence of too small S-D separations which do not actually sample the absorber and contribute only to the noise in the image. Localization error decreases with decreasing inter-optode distance as shown in Fig. 3.3b. The average of FWHM along the x- and y-directions (Table 3.1) is the highest for G1 and then plateaus for the increasing S-D density grid geometries (Fig. 3.4 a). Similarly, the ovality is highest for G1 and then plateaus for the grid S-D geometries. The overall results the location of this absorber indicate that G1 geometry may result in substantial distortions, but a grid geometry with a 2.2 cm separation can improve all of the computed image metrics, with only marginal gains for higher S-D densities. Absorber localization seems to be the most sensitive metric in terms of gains as one move to higher S-D densities. There were very marginal gains to be had when assuming layered tissue geometry versus a homogeneous one.

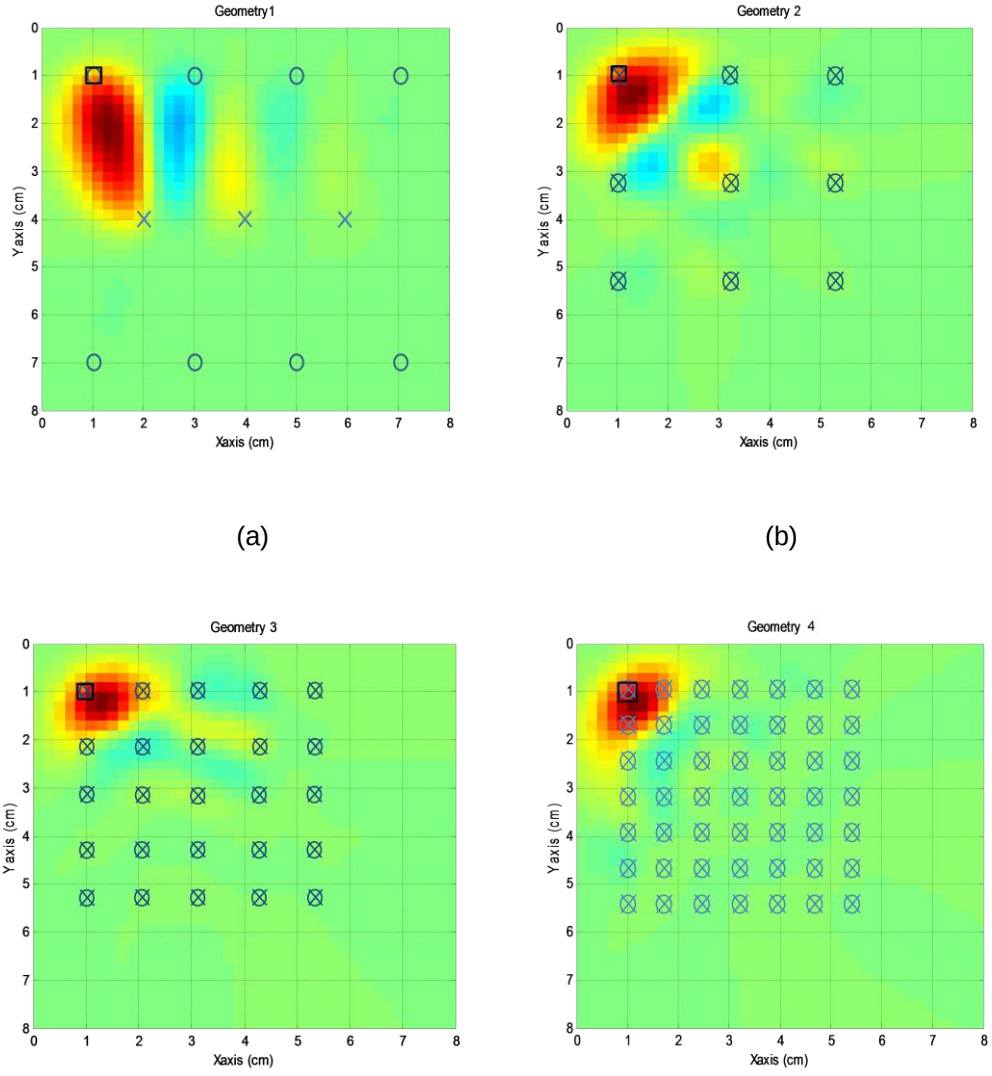

Figure 3.1 Reconstructed Images of Absorber 1 for a Homogenous Medium for Geometries (a) G-1, (b) G-2, (c) G-3 and (d) G-4

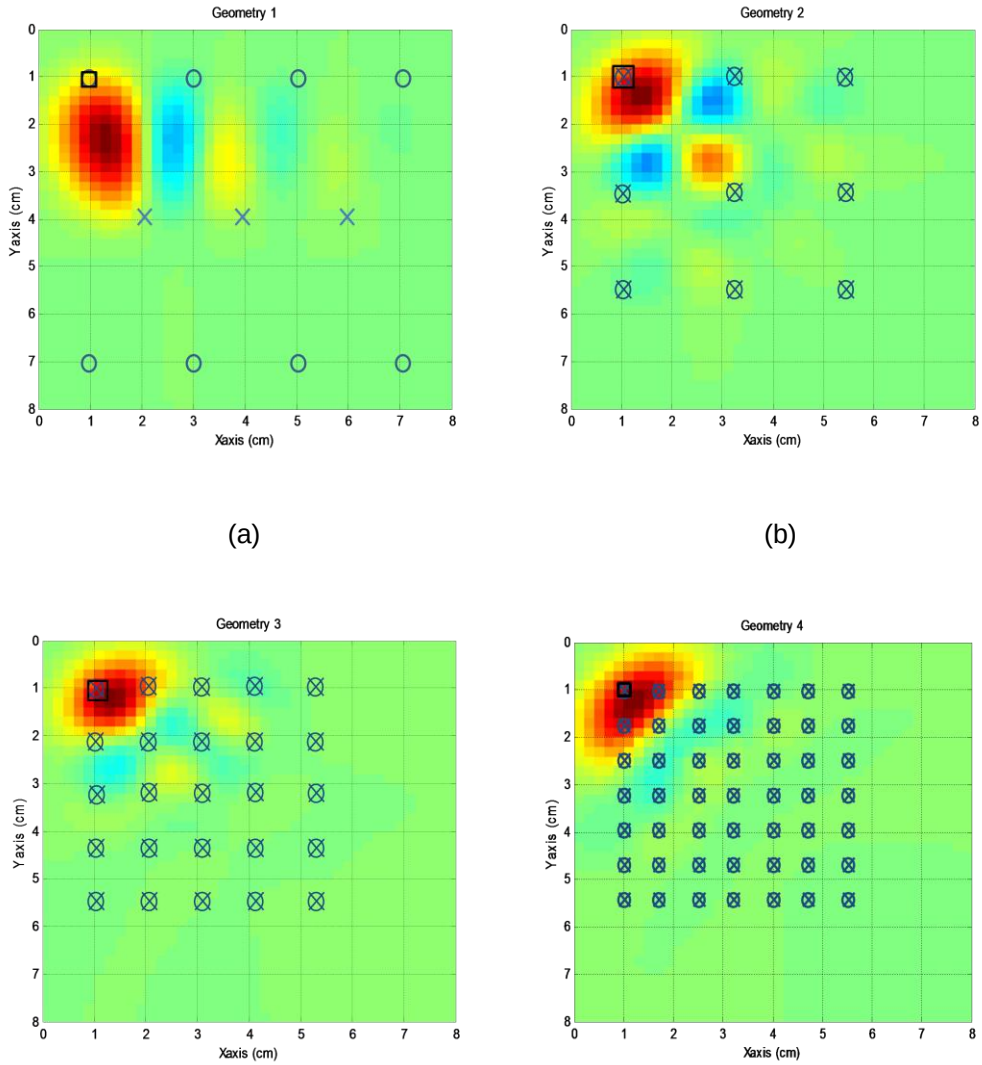

Figure 3.2 Reconstructed Images of Absorber 1 for a Layered Medium for Geometries (a) G-1, (b) G-2, (c) G-3 and (d) G-4

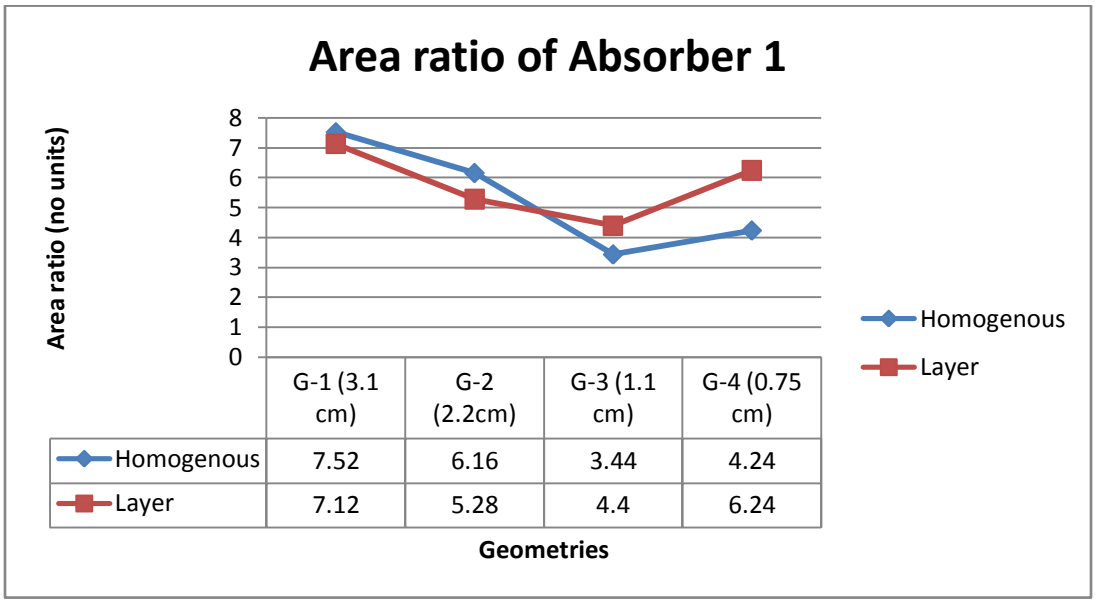

	G-1 (3.1 cm)	G-2 (2.2cm)	G-3 (1.1 cm)	G-4 (0.75 cm)
Homogenous	7.52	6.16	3.44	4.24
Layer	7.12	5.28	4.4	6.24

(a)

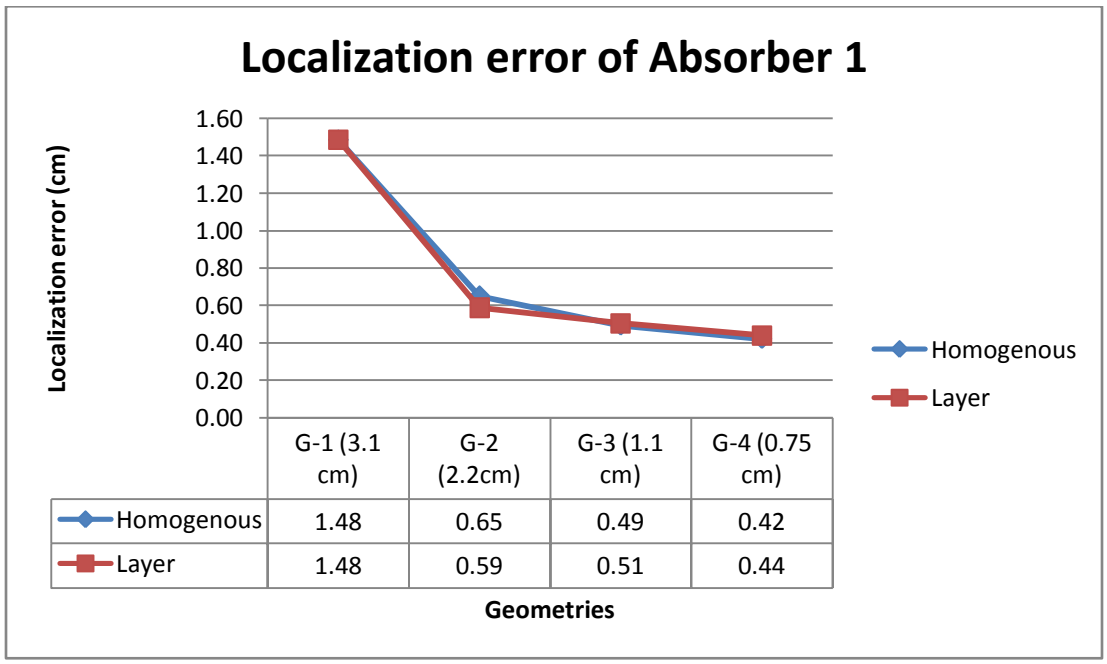

	G-1 (3.1 cm)	G-2 (2.2cm)	G-3 (1.1 cm)	G-4 (0.75 cm)
Homogenous	1.48	0.65	0.49	0.42
Layer	1.48	0.59	0.51	0.44

(b)

Figure 3.3 Comparison of Reconstructed Image Metrics for Anomaly 1 as Quantified by (a) Area Ratio (b) Localization error for

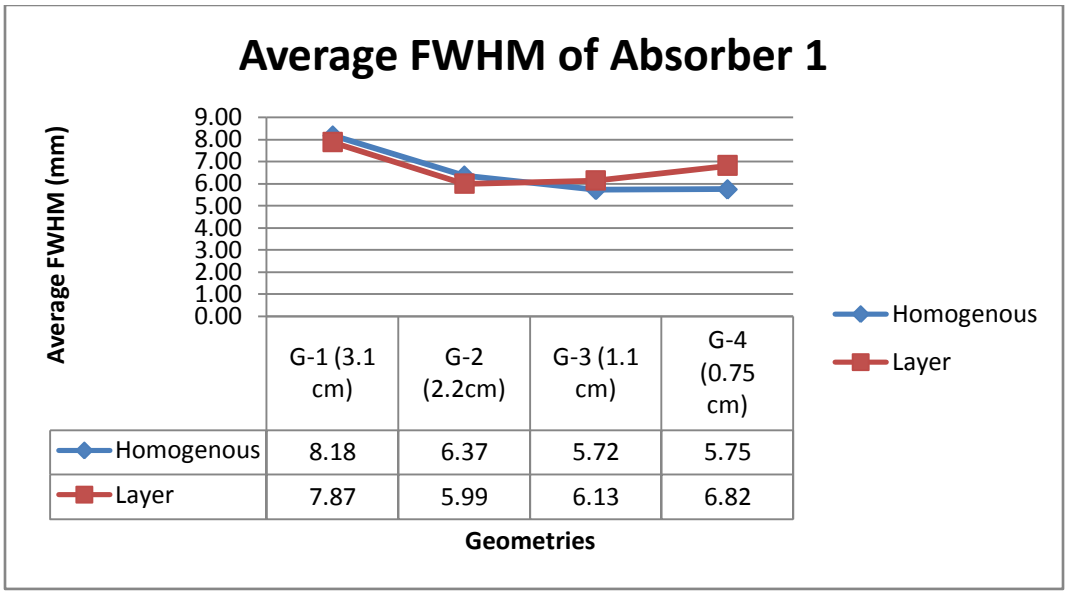

(a)

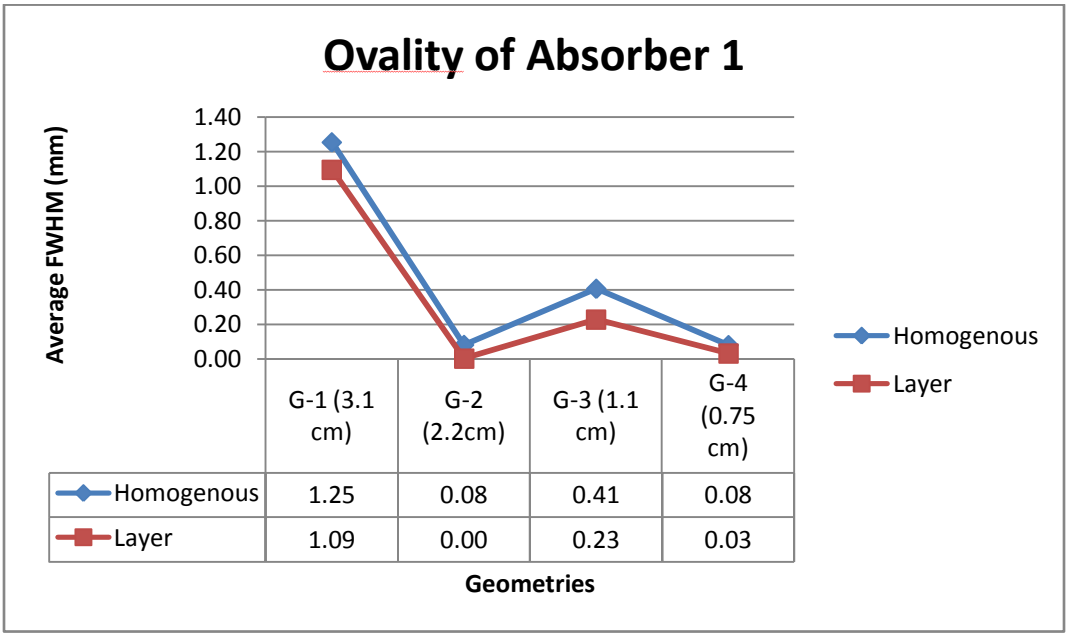

(b)

Figure 3.4 Comparison of Reconstructed Image Metrics for Anomaly 1 as quantified by (a) Average FWHM (b) Ovality for Homogeneous and Layered Media

Table 3.1 Comparison of FWHM along the X- and Y-Directions for Anomaly 1 for the Homogenous and Layered Medium for the Four S-D Geometries

Geometries	Homogenous medium		Layered medium	
	$FWHM_X$(mm)	$FWHM_Y$(mm)	$FWHM_X$(mm)	$FWHM_Y$(mm)
G-1	5.3	11.07	5.53	10.21
G-2	6.24	6.5	5.99	6
G-3	6.31	5.14	6.48	5.78
G-4	5.63	5.86	6.76	6.87

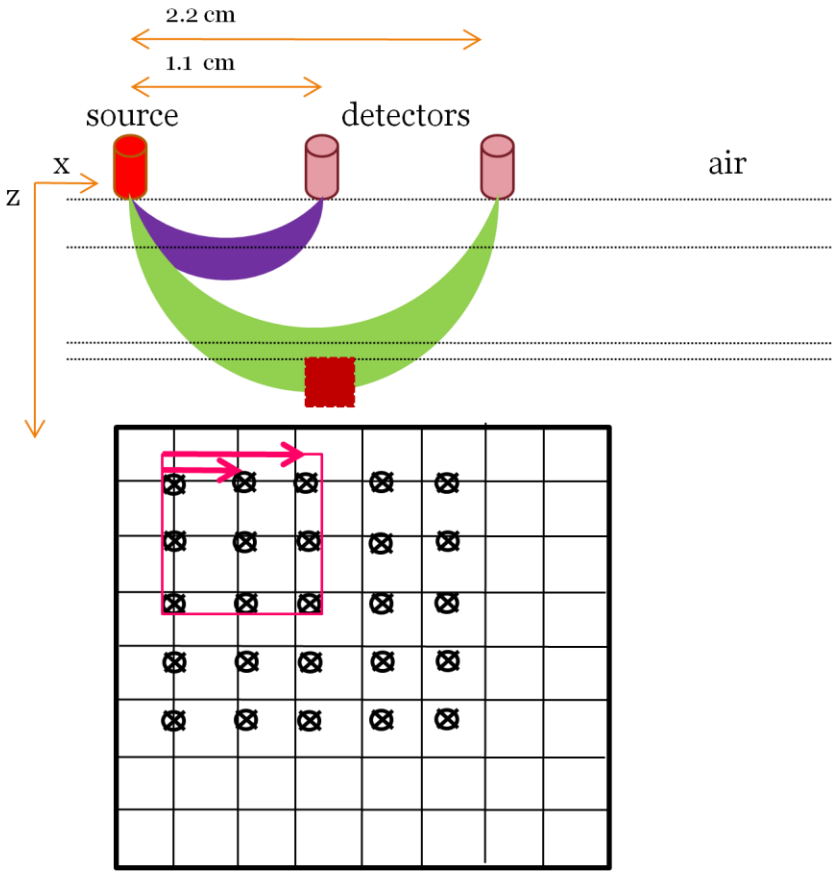

Figure 3.5 Schematic Diagram to Show the S-D pairs and their depth sampling for G-3 The red square represents the absorber. The pink arrows represent the S-D combinations considered whereas the pink square shows the detectors that are less than 3 cm from the 1st source.

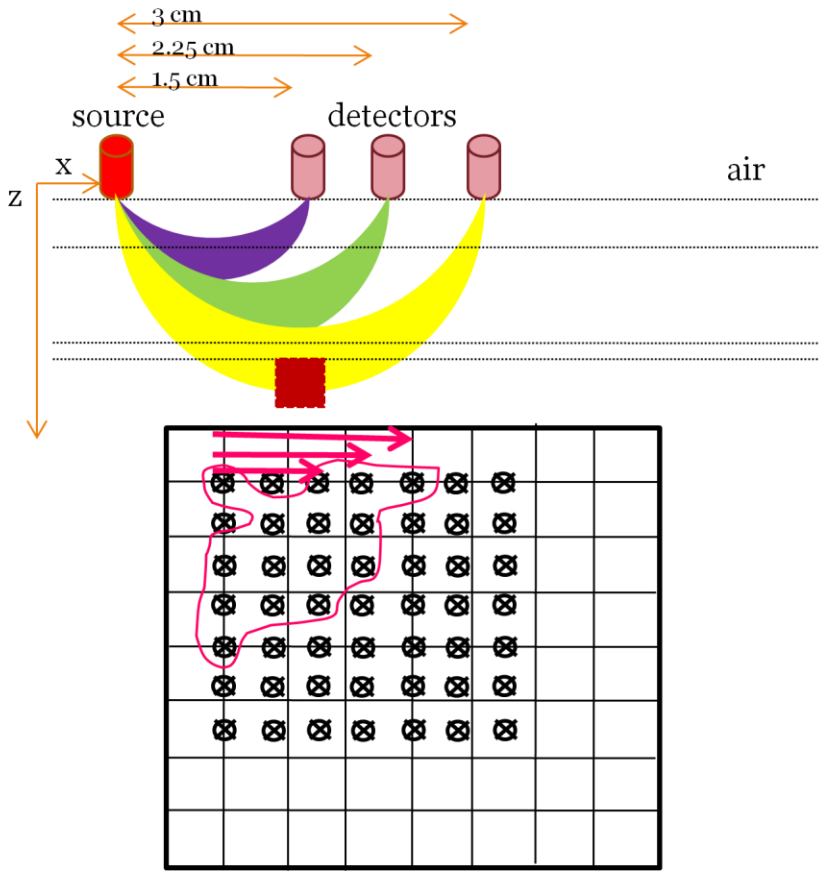

Figure 3.6 Schematic Diagram to Show the S-D pairs and their depth sampling for G-4. The red square represents the absorber. The pink arrows represent the S-D combinations considered whereas the irregular pink outline shows the detectors that are less than 3 cm from the 1st source.

The reason for the increase in the area ratio for the geometry G-4 is indicated in the above figure: For higher S-D density geometries there are larger numbers of S-D pairs that do not actually sample the depth in which the absorber was placed in (grey matter). These S-D pairs therefore only contributed additional noise to the fNIRS data, which then result in more noise and larger size absorbers in the reconstructed images.

3.1.2 Anomaly 2

The reconstructed images for Anomaly 2 (black-edged square located below a detector at the center of the FOV in Figs 3.4 and 3.5) for different optode geometries were compared for the homogenous and layered medium tissues.

The G1 geometry was by far the most vulnerable to distortions in the reconstructed images for that absorber location as the absorber can be projected along diagonals linking the 4 nearest detectors. For the G2 through G4 grid geometries, the reconstructed activation region was more localized and shrunk to its smallest value for an S-D density of 1.1 cm (Fig. 3.7c). As discussed previously the activation size increased for G4 due to the increased noise for multiple S-D pairs not sampling the activation region. In terms of the reconstructed image metrics, area ratio (Fig. 3.9a) improved down to an S-D spacing of 1.1 cm though the absorber localization error was always small for all S-D geometries (Fig. 3.9b) with some variations due to noise in the image affecting the detailed shape and size of the reconstructed activation region. Similarly, the average FWHM (Fig. 3.10a and Table 3.2) and ovality (Fig. 3.10b) improved the most for an S-D separation of 1.1 cm. There were no obvious gains in moving from a homogeneous medium geometry to a layered medium one.

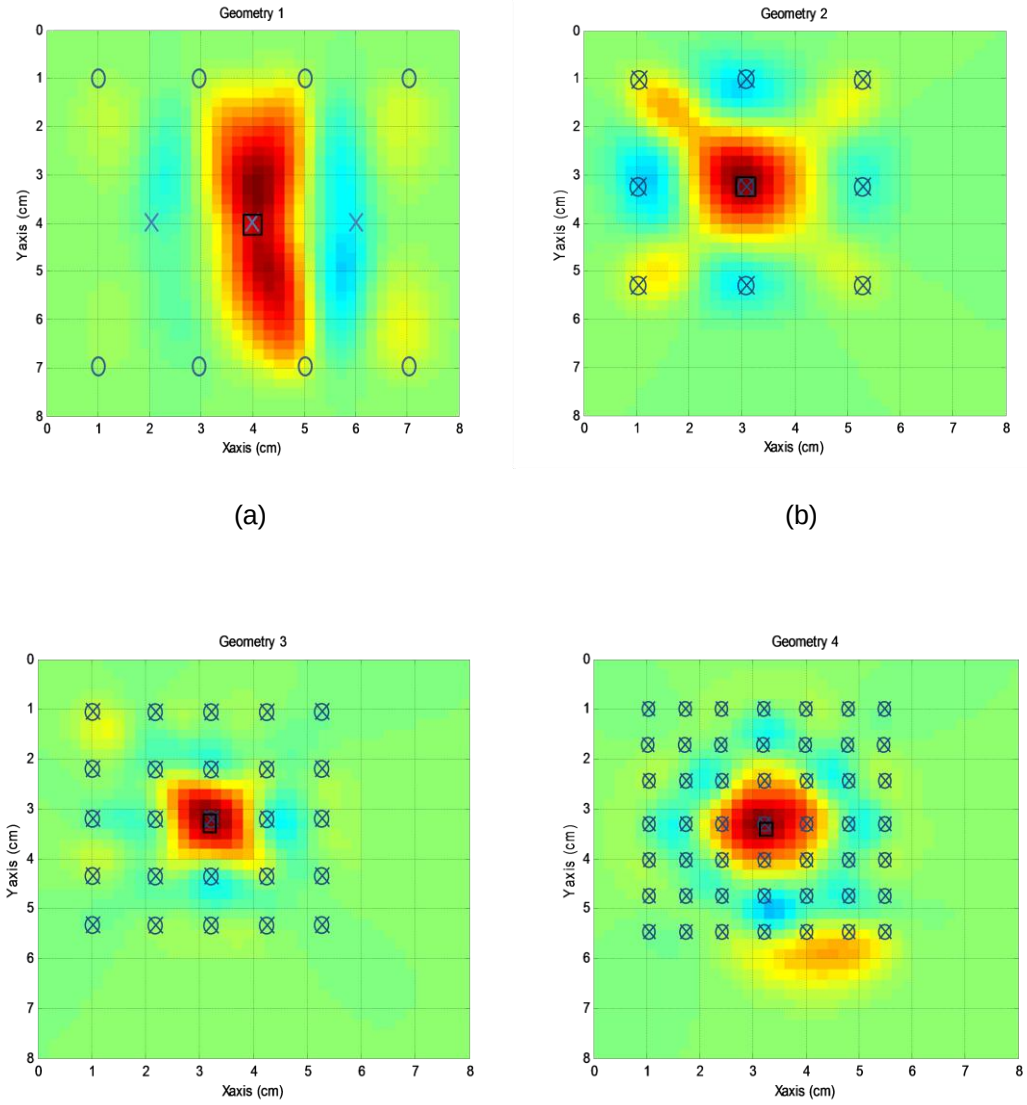

Figure 3.7 Reconstructed Images of Absorber 1 of Homogenous Medium for Geometries (a) G-1, (b) G-2, (c) G-3 and (d) G-4

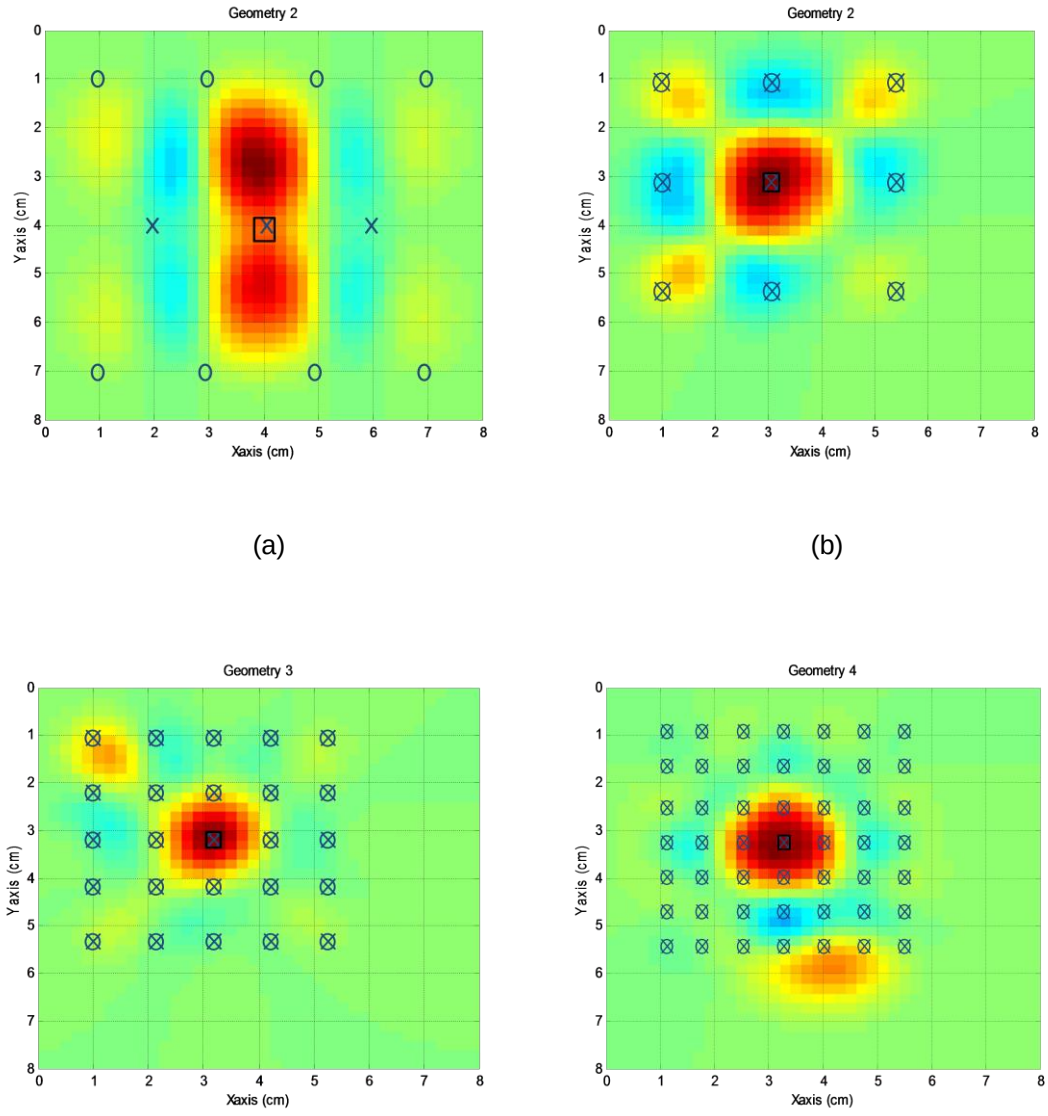

Figure 3.8 Reconstructed Images of Absorber 2 of Layered Medium for Geometries (a) G-1, (b) G-2, (c) G-3 and (d) G-4

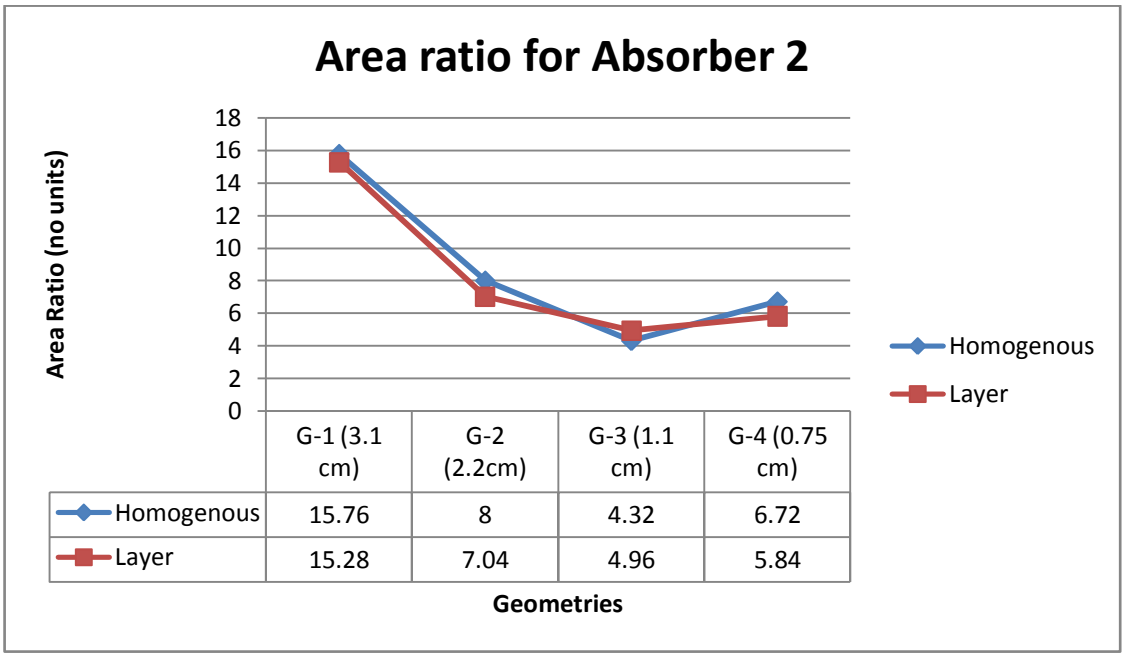

(a)

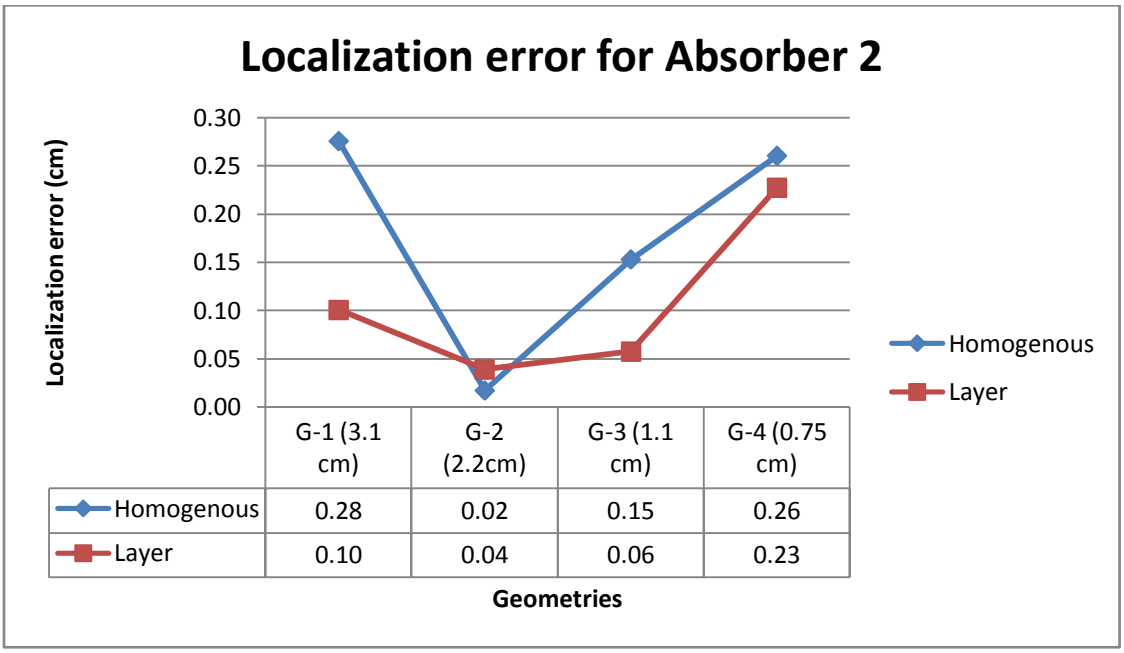

(b)

Figure 3.9 Comparison of Reconstructed Image Metrics for Anomaly 2 as quantified by (a) Area Ratio (b) Localization error for Homogeneous and Layered Media

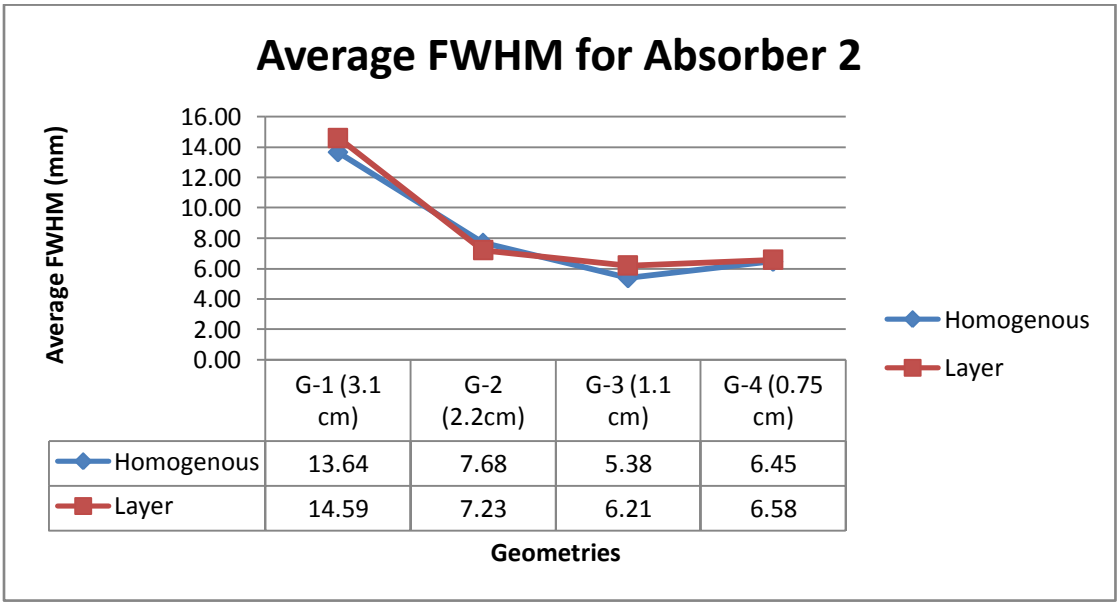

(a)

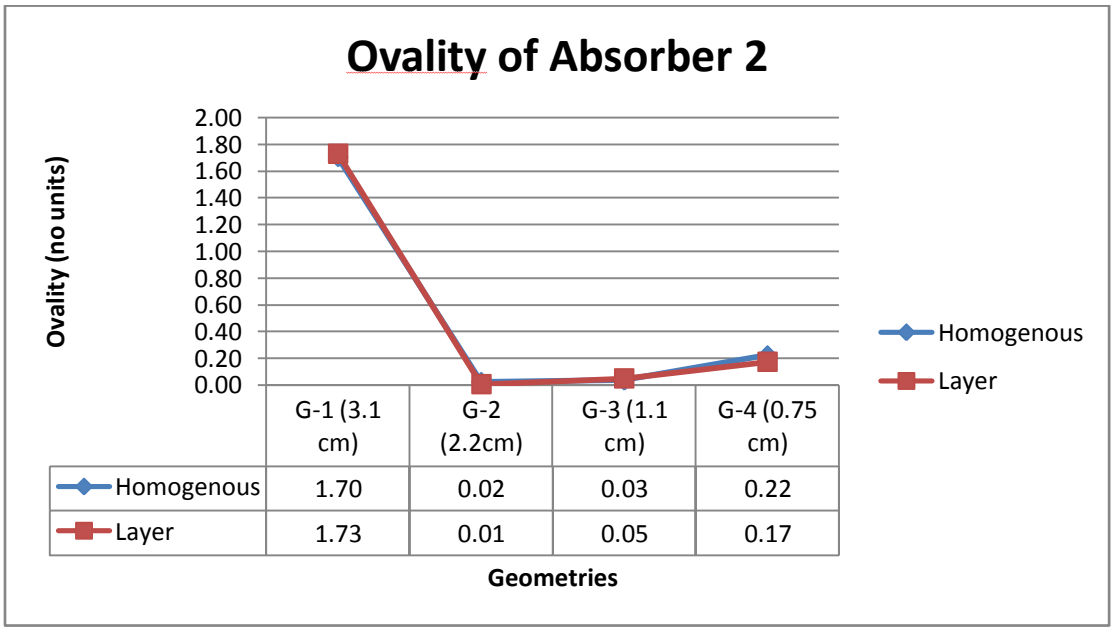

(b)

Figure 3.10 Comparison of Reconstructed Image Metrics for Anomaly 2 as quantified by (a) Average FWHM (b) Ovality for Homogeneous and Layered Media

Table 3.2 Comparison of FWHM along the X- and Y-Directions for Anomaly 2 for the Homogenous and Layered Medium for the Four S-D Geometries

Geometries	Homogenous medium		Layered medium	
	$FWHM_X$(mm)	$FWHM_Y$(mm)	$FWHM_X$(mm)	$FWHM_Y$(mm)
G-1	6.02	21.25	6.19	22.99
G-2	7.64	7.72	7.22	7.23
G-3	5.42	5.33	6.14	6.29
G-4	6.81	6.10	6.87	6.30

3.1.3 Anomaly 3

The reconstructed images of Anomaly 3 (black-edged square located at the intersection between two diagonals linking nearest neighbor S-D pairs, Figs 3.11 and 3.12) for different optode geometries were compared for the homogenous and layered medium tissues.

The overall trend of the findings is similar to those for Anomaly 1 and Anomaly 2, above. Interestingly, the metrics quantified from the reconstructed images (Figure 3.13a,b and Figure 3.13 a,b) indicate that for this absorber location there are some minor differences between the homogeneous and layered media geometries. The higher A-matrix values for the layered geometry resulted in higher sensitivity for this absorber location that is by multiple S-D pairs. The higher sensitivity resulted in higher reconstructed absorber values and therefore to larger activation area size and FWHM. These results indicate that the apparent absorber size has a weak dependence on the tissue geometry in regions of the reconstructed image that are sampled with higher detection sensitivity. Counter-intuitively, the layered model of photon transport results in slightly larger absorber sizes in this case, due to its larger A-matrix values compared to the homogeneous geometry, even though it is a more accurate model of photon transport than the latter.

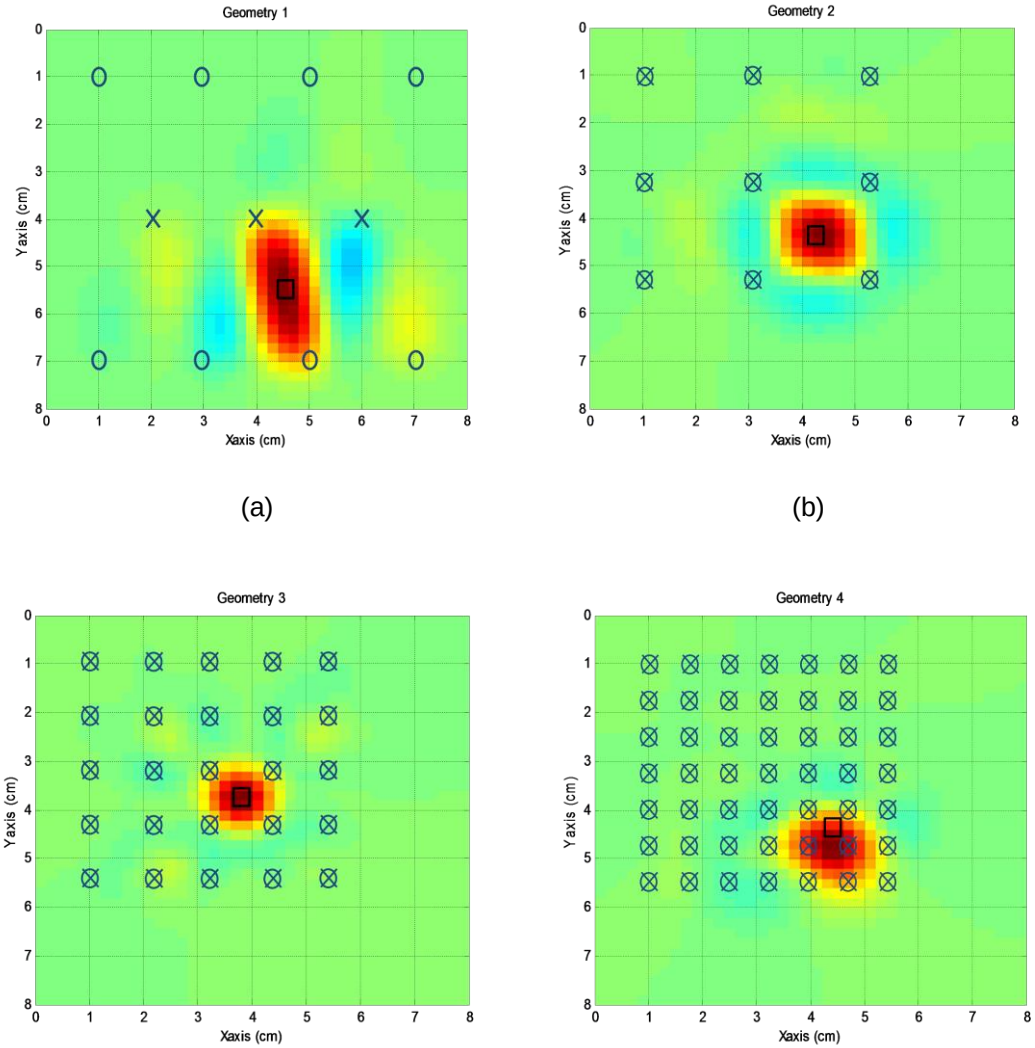

Figure 3.11 Reconstructed Images of Absorber 3 of Homogenous Medium for Geometries (a) G-1, (b) G-2, (c) G-3 and (d) G-4

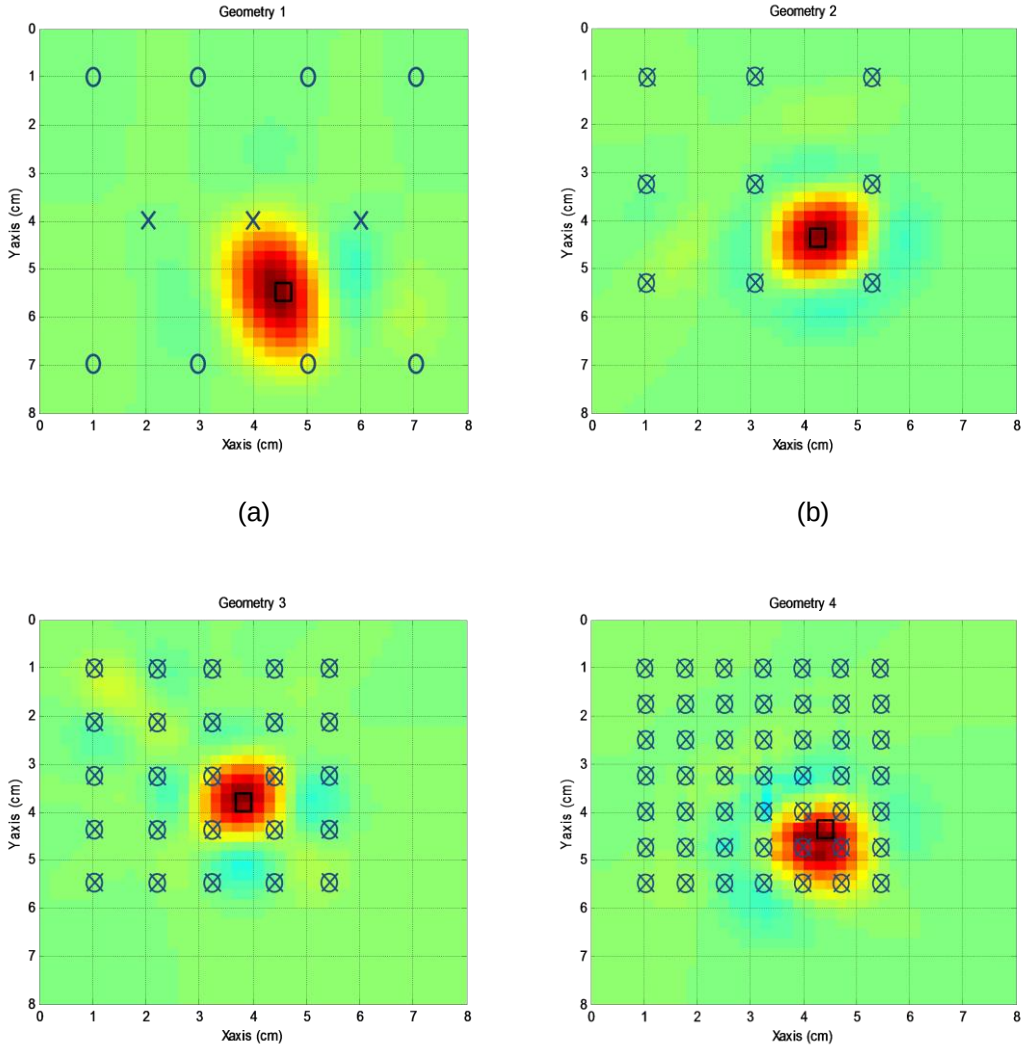

Figure 3.12 Reconstructed Images of Absorber 3 of Layered Medium for Geometries (a) G-1, (b) G-2, (c) G-3 and (d) G-4

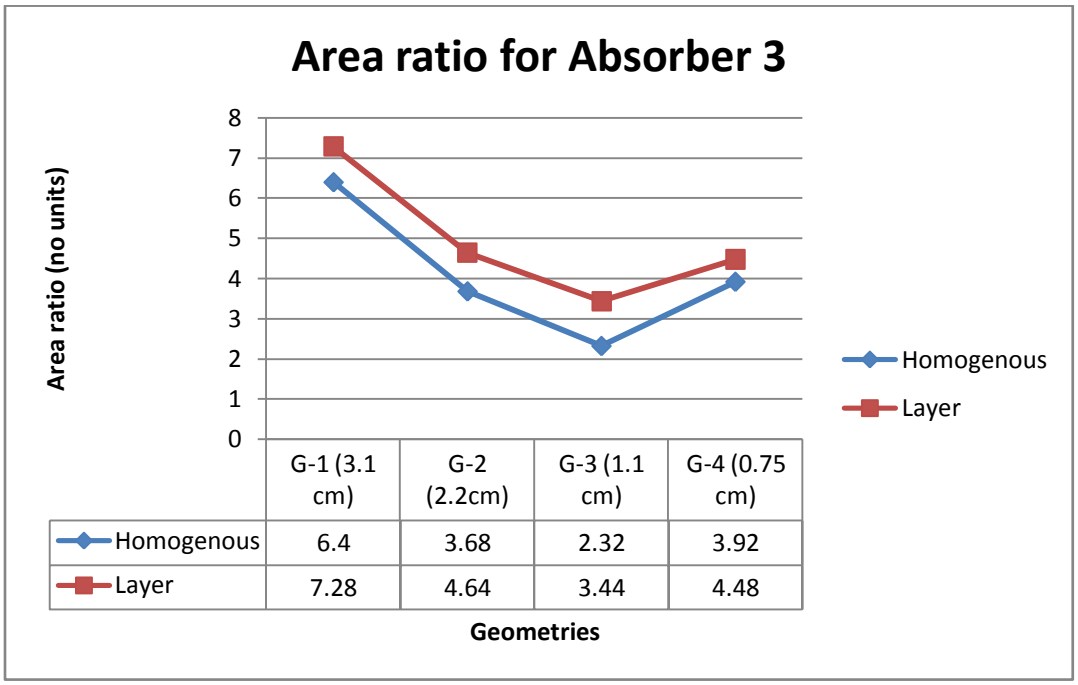

(a)

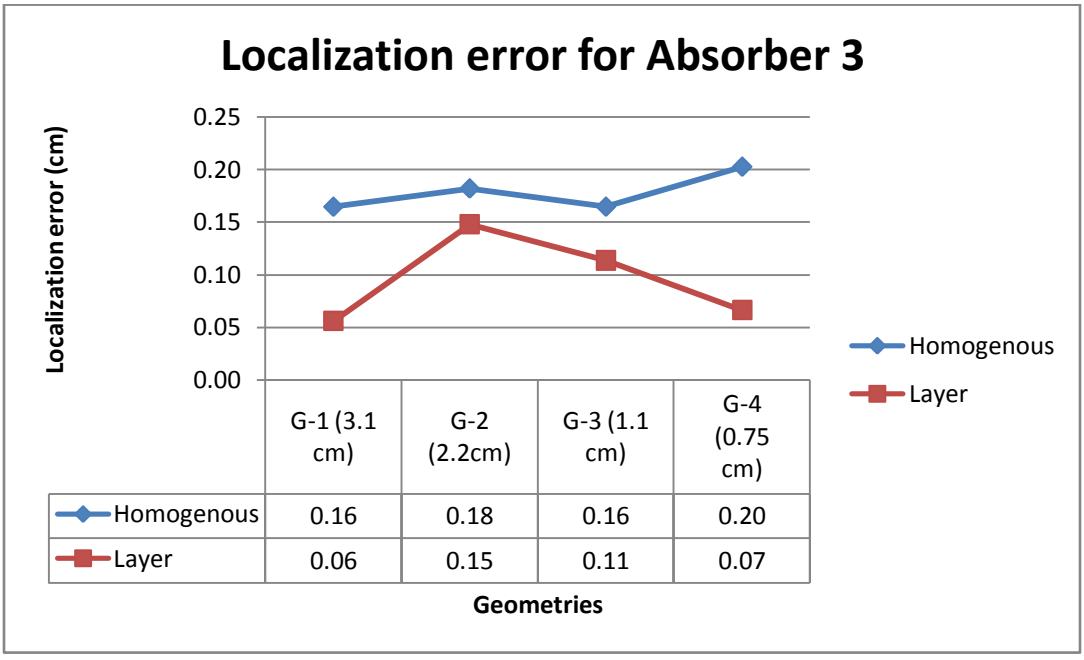

(b)

Figure 3.13 Comparison of Reconstructed Image Metrics for Anomaly 3 as quantified by (a) Area Ratio (b) Localization error for Homogeneous and Layered Media

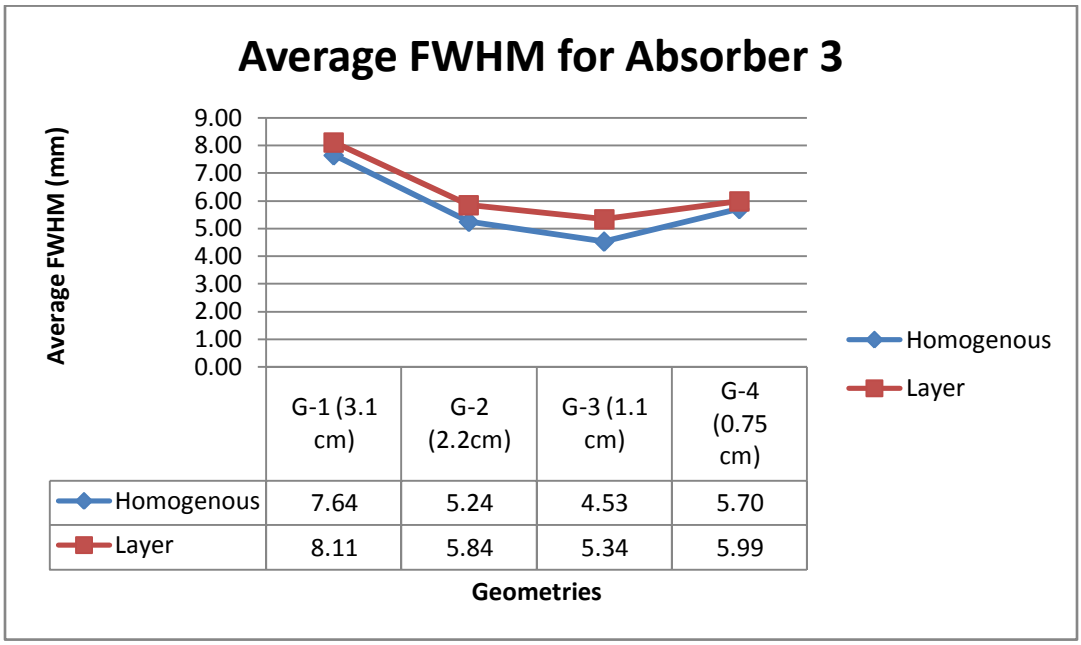

(a)

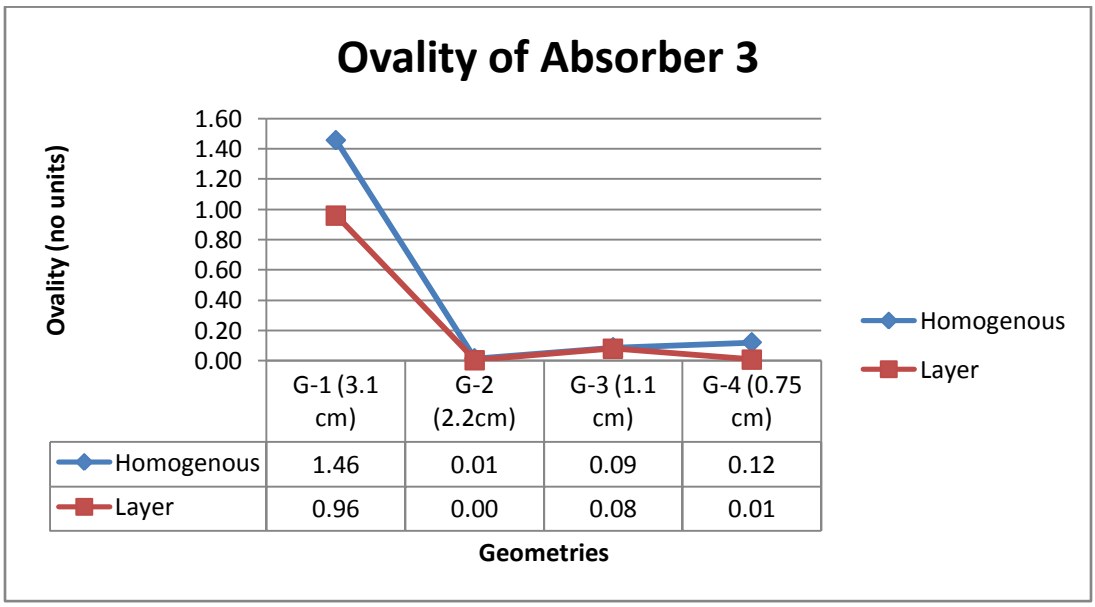

(b)

Figure 3.14 Comparison of Reconstructed Image Metrics for Anomaly 3 as quantified by (a) Average FWHM (b) Ovality for Homogeneous and Layered Media

Table 3.3 Comparison of FWHM along the X- and Y-Directions for Anomaly 3 for the Homogenous and Layered Medium for the Four S-D Geometries

Geometries	Homogenous medium		Layered medium	
	$FWHM_X$(mm)	$FWHM_Y$(mm)	$FWHM_X$(mm)	$FWHM_Y$(mm)
G-1	4.34	10.94	6.04	10.17
G-2	5.22	5.26	5.85	5.84
G-3	4.62	4.43	5.23	5.45
G-4	5.87	5.53	6.00	5.98

3.1.4 A-matrix of homogenous and layered medium

To explain the reason for which the reconstructed images looked qualitatively similar for the homogenous and layered media tissue backgrounds, a 2-D plot of the 3-D sensitivity (A-matrix values in the 'banana' intersecting by the line shown in Figure 3.15a) is shown in Figure 3.15b. The latter figure shows that there is an increase in amplitude of the sensitivity for layered media but there is no substantial change in the overall shape of this 'banana' cross-section. Thus the spatial resolution, which depends on the width of these curves, does not change much between the homogenous and the layered media geometries. More specifically, the entire reconstructed image appears to be multiplied by a scalar factor, which changes the FWHM values, but a linear operation such a multiplication would not change the ability to resolve two absorbers placed in close vicinity to each other (e.g. as is done for Rayleigh's criterion).

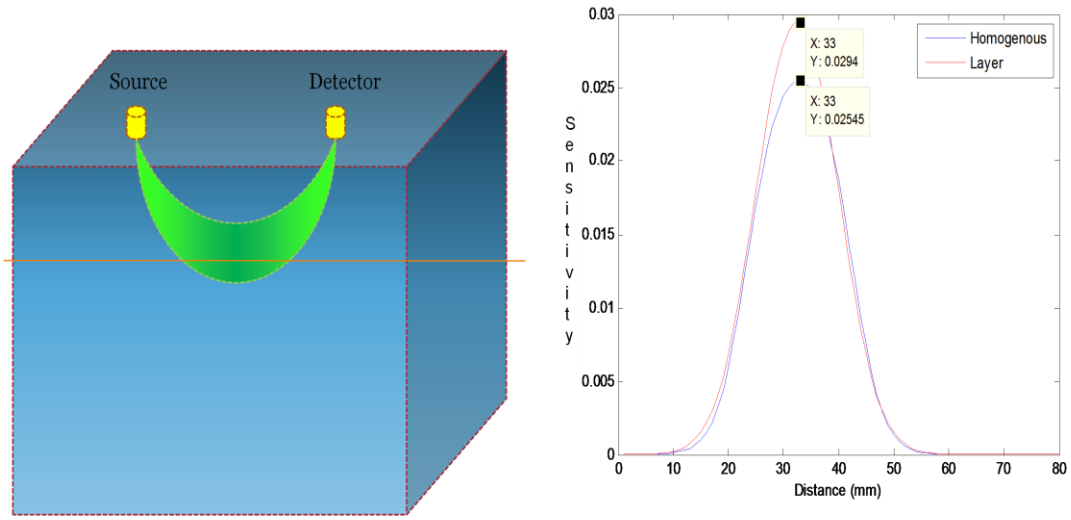

(a) (b)

Figure 3.15 Sensitivity profile (a) shown on a 3-D tissue block (b) A plot of the sensitivity profile along the x-axis at the midpoint of the source and the detector for the homogenous and layered medium

3.2 Effect of Wrongly Assumed Background Optical Properties on Reconstructed Images

It is difficult to know the optical properties of the head of each patient and it is therefore important to assess the effect of assuming wrong optical properties for different head tissues on the resulting reconstructed images. As prior work has assessed the effect of μ_a in the reconstructed images [32] this work has focused on the effect of wrongly assumed μ_s' for the background tissues. The effect of μ_s' was considered as important to investigate as its value is substantially larger than that of μ_a in tissues. Given that the knowledge in background optical property values for μ_s' varies considerably for all tissue types in the head [24, 32, and 33] the size of perturbations considered were ±50% and ±25% away for the previously assumed baseline values.

3.2.1 Anomaly 1

In order to compare differences in reconstructed image metrics with respect to corresponding baseline values results in all figures below are plotted as a ratio with respect to the baseline values. The ratio of activation area ratios indicates variability of only a few percent even for 50% deviations in μ_s' for both homogeneous (Fig. 3.10a) and layered (Fig. 3.10b) media. Higher sensitivity in background optical properties was only seen in G1. The localization error for the homogenous medium (Fig. 3.11a) across all the S-D geometries does not vary more than 7% for perturbations from -50% to +50%. In contrast, the layered medium (Fig. 3.11b) showed higher sensitivity to the assumed background optical properties and increasingly so for higher errors in μ_s'. The ovality appeared to be a relatively robust metric for both a homogenous medium (Fig. 3.12a) and a layered medium (Fig. 3.12b) for all S-D geometries, though Monte Carlo noise was responsible for some exceptions.

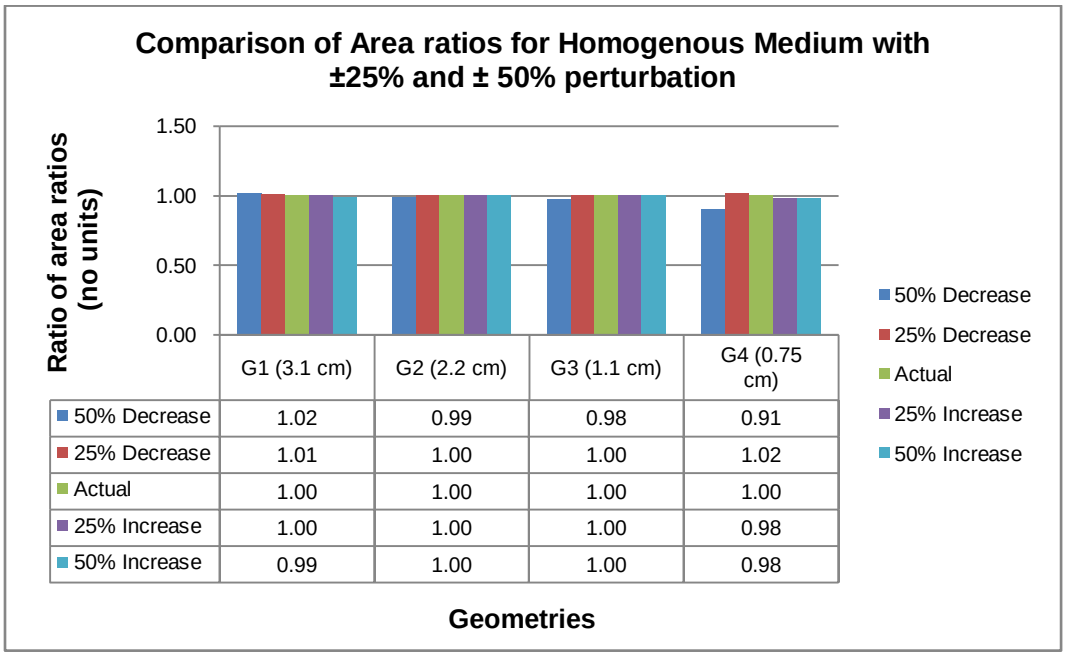

(a)

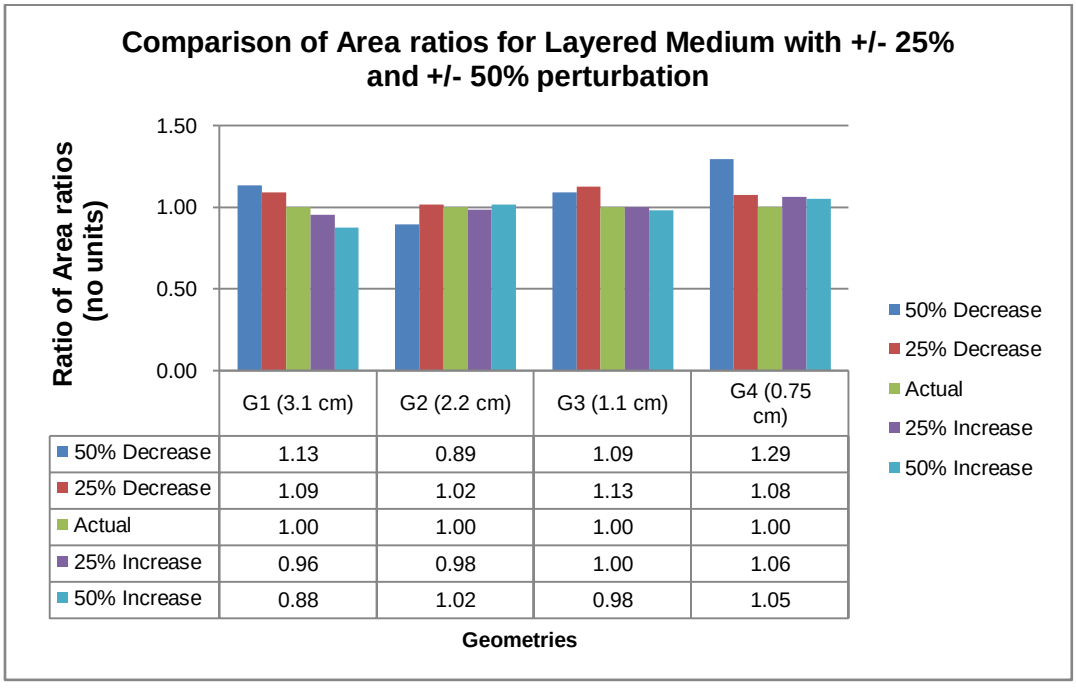

(b)

Figure 3.16 Comparisons of Ratio of Area Ratios Across Four Optode Geometries for Anomaly 1(a) Homogenous Medium, (b) Layered Medium

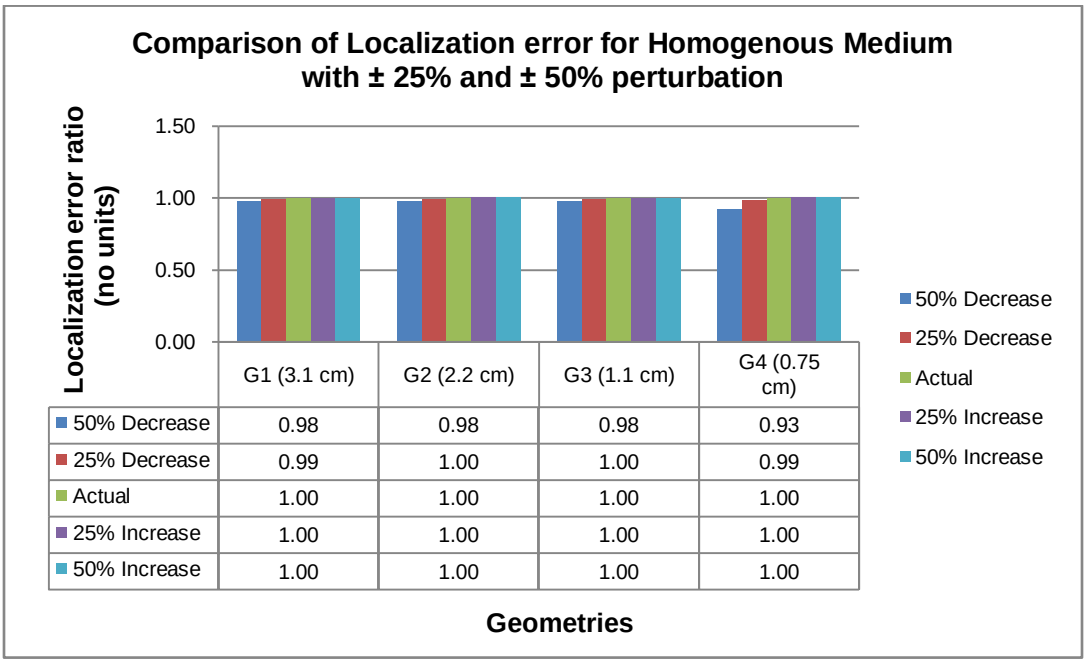

(a)

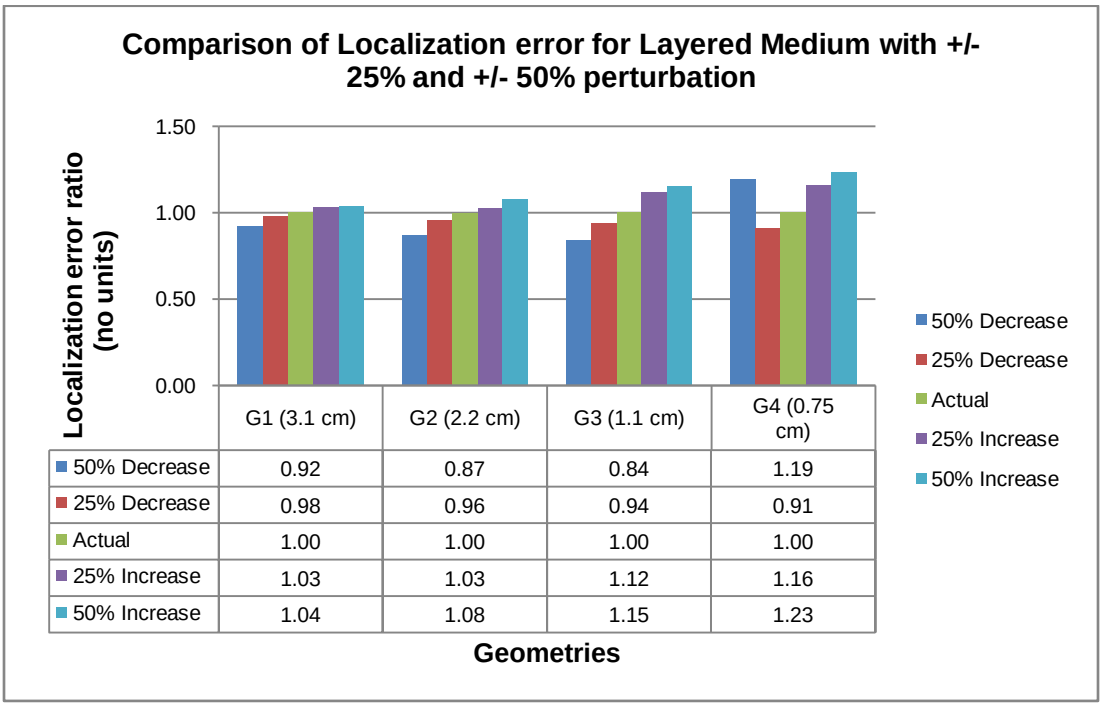

(b)

Figure 3.17 Comparisons of Localization Error Ratios Across Four Optode Geometries for Anomaly 1 (a) Homogenous Medium, (b) Layered Medium

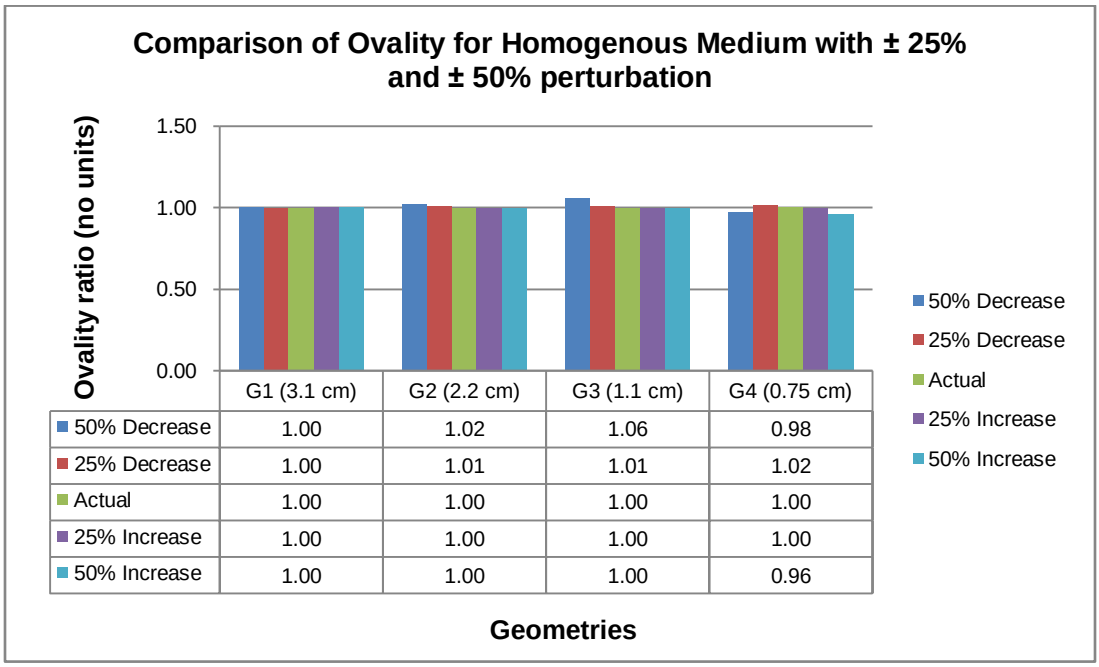

(a)

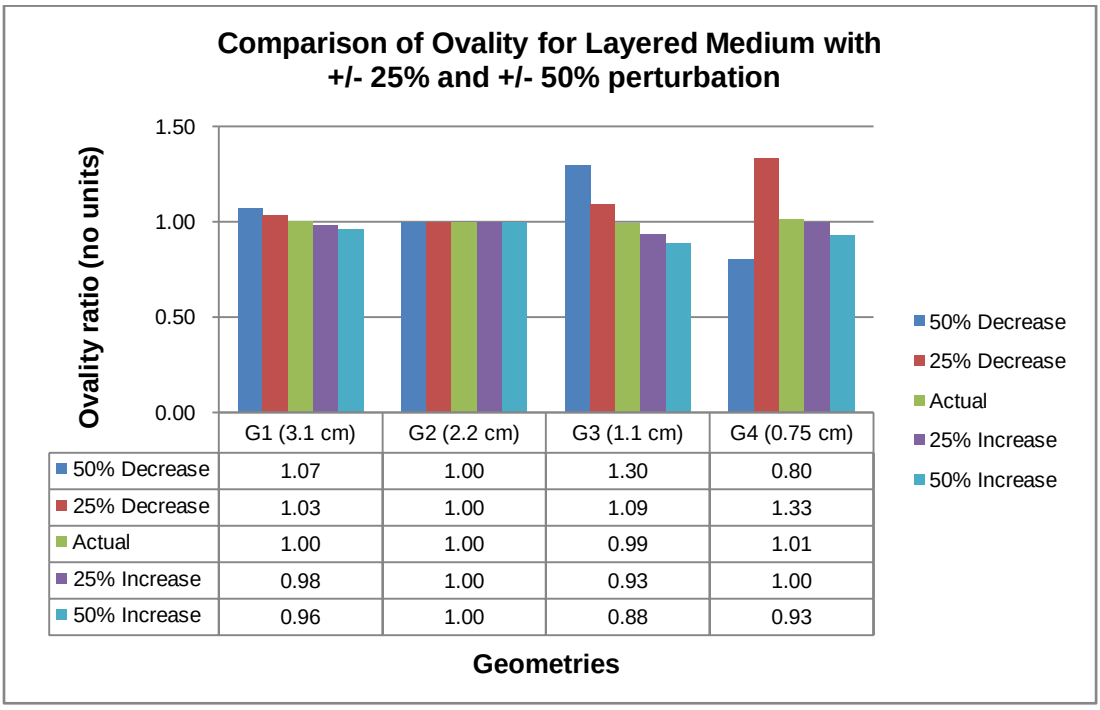

(b)

Figure 3.18 Comparisons of Ovality Ratios Across Four Optode Geometries for Anomaly 1 (a) Homogenous Medium, (b) Layered Medium

3.2.2 Anomaly 2 and Anomaly 3

Similar to the results for Anomaly 1, the reconstructed images for Anomaly 2 (Figures. 3.19-3.21) and Anomaly 3 (Figures. 3.22-3.24) varied little when a homogenous tissue model was assumed. In contrast, similar to the results for Anomaly 1, for layered tissue geometry the reconstructed images for Anomaly 2 and 3 showed substantial dependence on the assumed background optical properties. Though the ratio of ovality shows a large variation for the layered medium (G-2 and G-3 for Anomaly 2, G-3 G-4 for Anomaly 3), the absolute ovality values are very small (table 3.4, 3.5). In ongoing work it is being verified, by comparison with Monte Carlo simulated reflectance results, whether this variability is due to the layered geometry itself or the numerical instabilities in the diffusion equation solver for that tissue geometry.

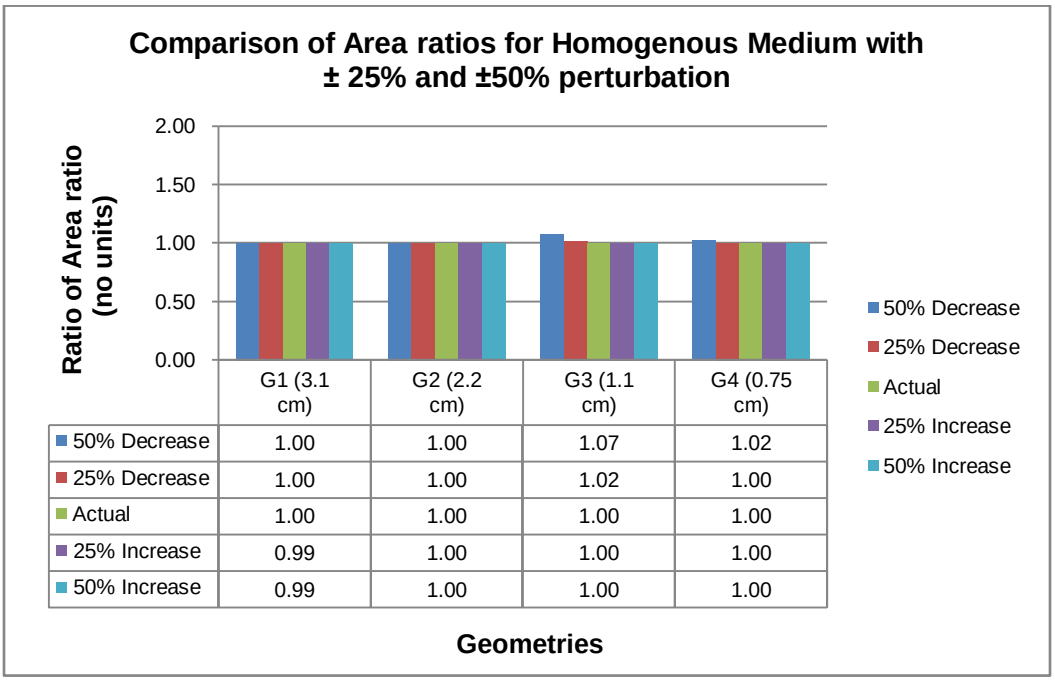

(a)

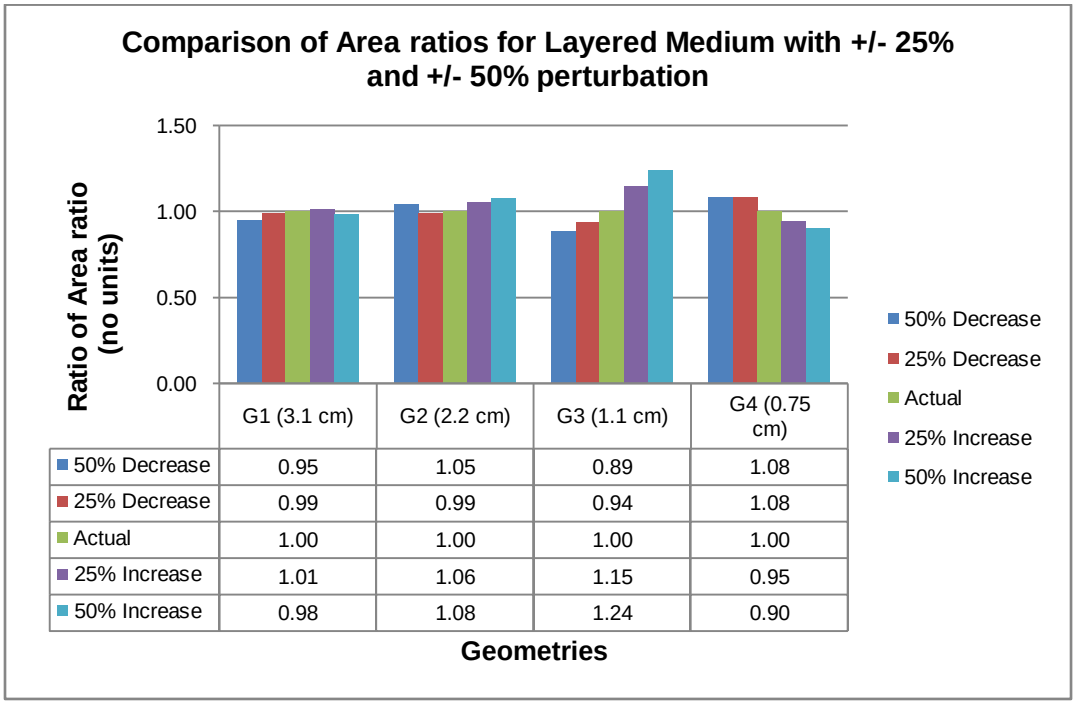

(b)

Figure 3.15 Comparisons of Ratio of Area Ratios across Four Optode Geometries for Anomaly 2 (a) Homogenous Medium, (b) Layered Medium

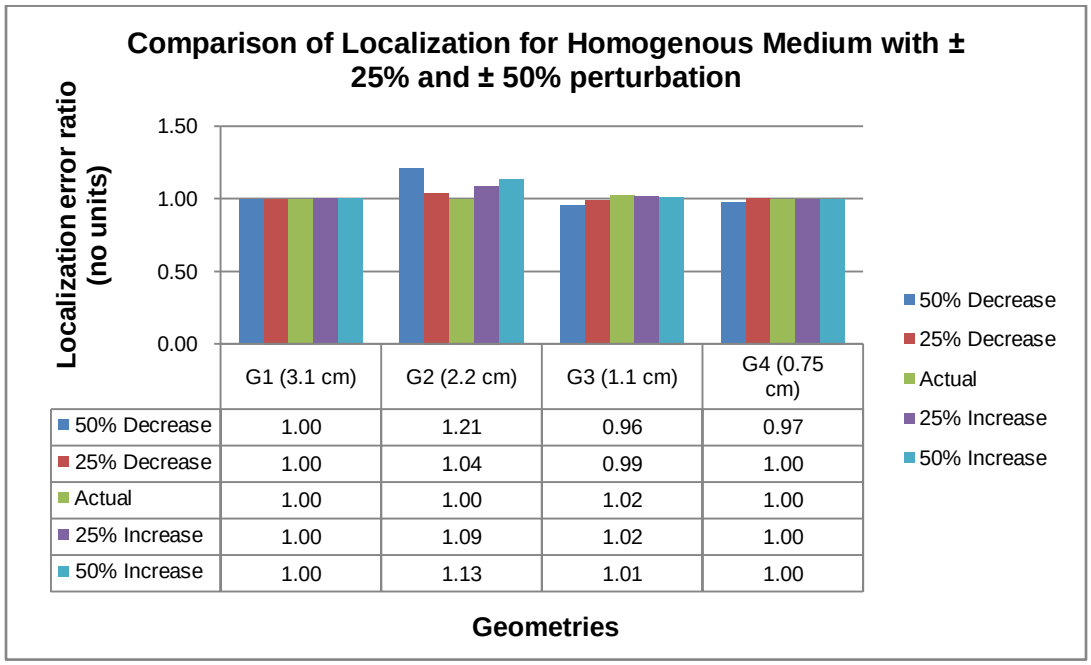

(a)

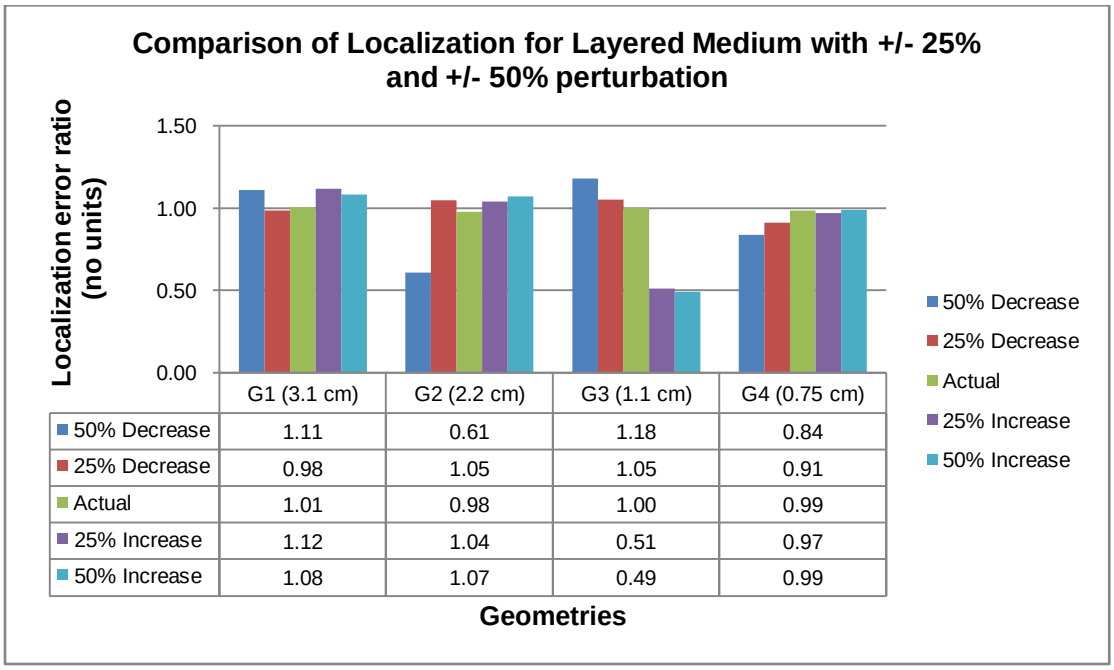

(b)

Figure 3.16 Comparisons of Localization Error Ratios across Four Optode Geometries for Anomaly 2 (a) Homogenous Medium, (b) Layered Medium

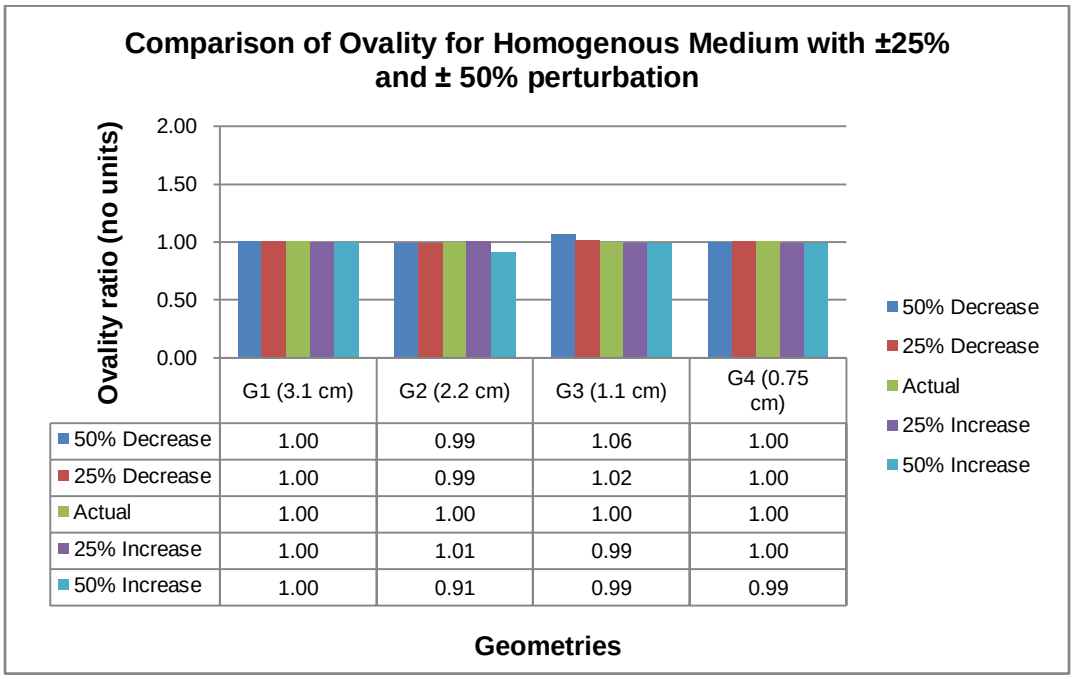

(a)

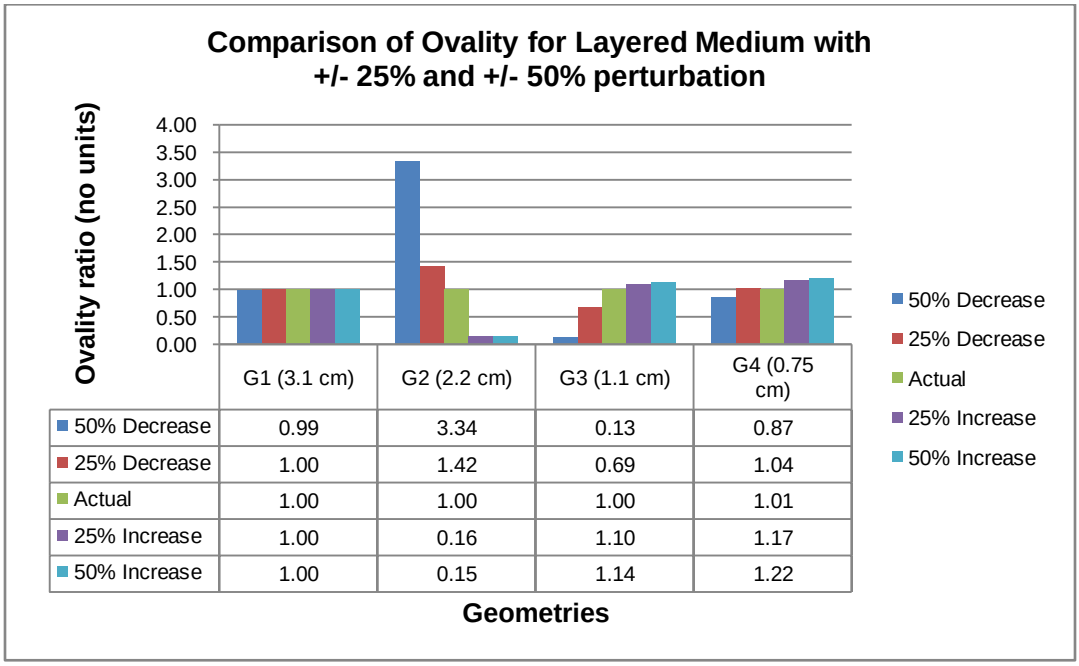

(b)

Figure 3.17 Comparisons of Ovality Ratios across Four Optode Geometries for Anomaly 2 (a) Homogenous Medium, (b) Layered Medium

Table 3.4 Summary of Ovality for G-2 and G-3 under Different Perturbation Conditions

Geometry	%Perturbation	Ovality (no unit)	Baseline (no unit)	Ratio (no unit)
G-2	50% Decrease	1.68E-02	5.04E-03	3.34
	25% Decrease	7.18E-03	5.04E-03	1.42
	Baseline	5.04E-03	5.04E-03	1
	25% Increase	7.83E-04	5.04E-03	0.16
	50% Increase	7.75E-04	5.04E-03	0.15
G-3	50% Decrease	6.27E-03	4.77E-02	0.13
	25% Decrease	3.28E-02	4.77E-02	0.69
	Baseline	4.77E-02	4.77E-02	1
	25% Increase	5.23E-02	4.77E-02	1.1
	50% Increase	5.46E-02	4.77E-02	1.14

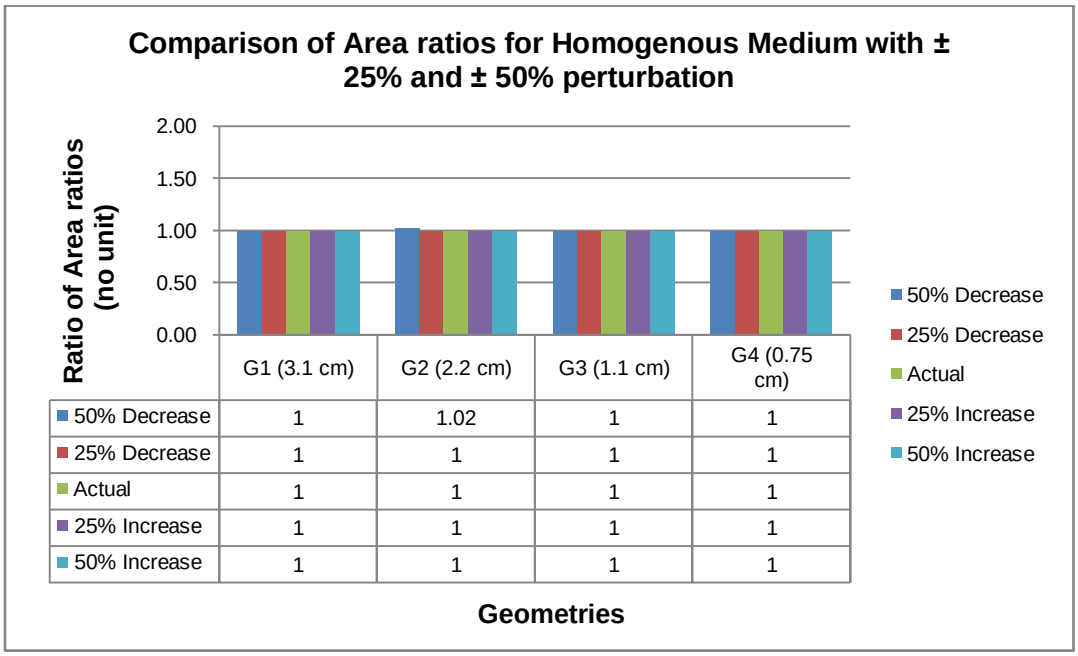

	G1 (3.1 cm)	G2 (2.2 cm)	G3 (1.1 cm)	G4 (0.75 cm)
50% Decrease	1	1.02	1	1
25% Decrease	1	1	1	1
Actual	1	1	1	1
25% Increase	1	1	1	1
50% Increase	1	1	1	1

(a)

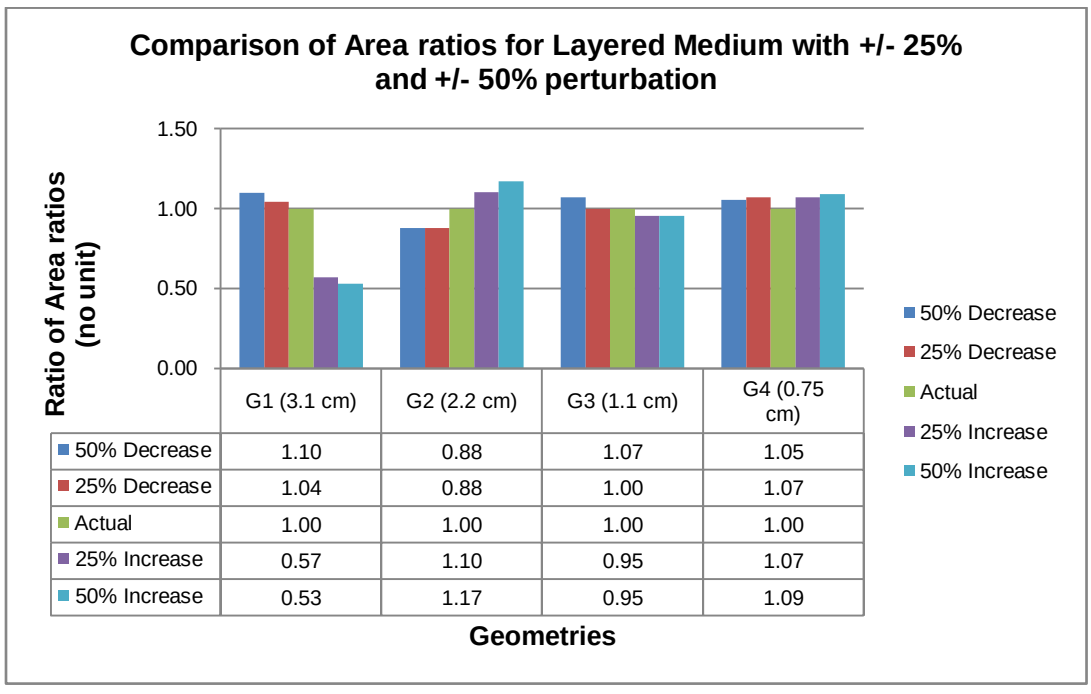

	G1 (3.1 cm)	G2 (2.2 cm)	G3 (1.1 cm)	G4 (0.75 cm)
50% Decrease	1.10	0.88	1.07	1.05
25% Decrease	1.04	0.88	1.00	1.07
Actual	1.00	1.00	1.00	1.00
25% Increase	0.57	1.10	0.95	1.07
50% Increase	0.53	1.17	0.95	1.09

(b)

Figure 3.18 Comparisons of Ratio of Area Ratios across Four Optode Geometries for Anomaly 3 (a) Homogenous Medium, (b) Layered Medium

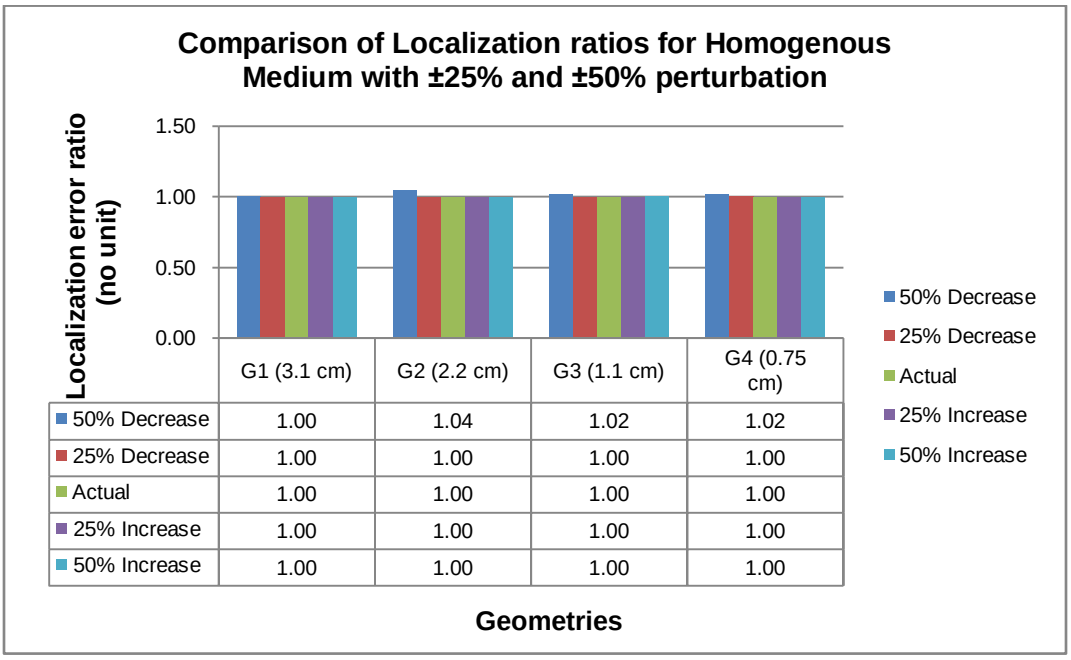

(a)

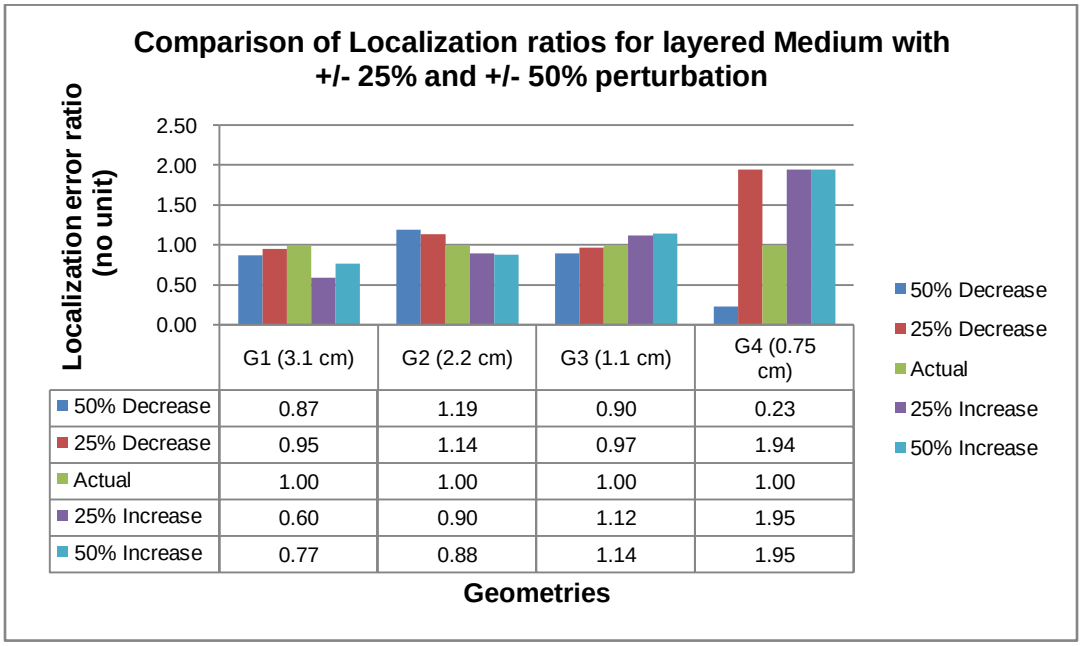

(b)

Figure 3.19 Comparisons of Localization Error Ratios across Four Optode Geometries for Anomaly 3 (a) Homogenous Medium, (b) Layered Medium

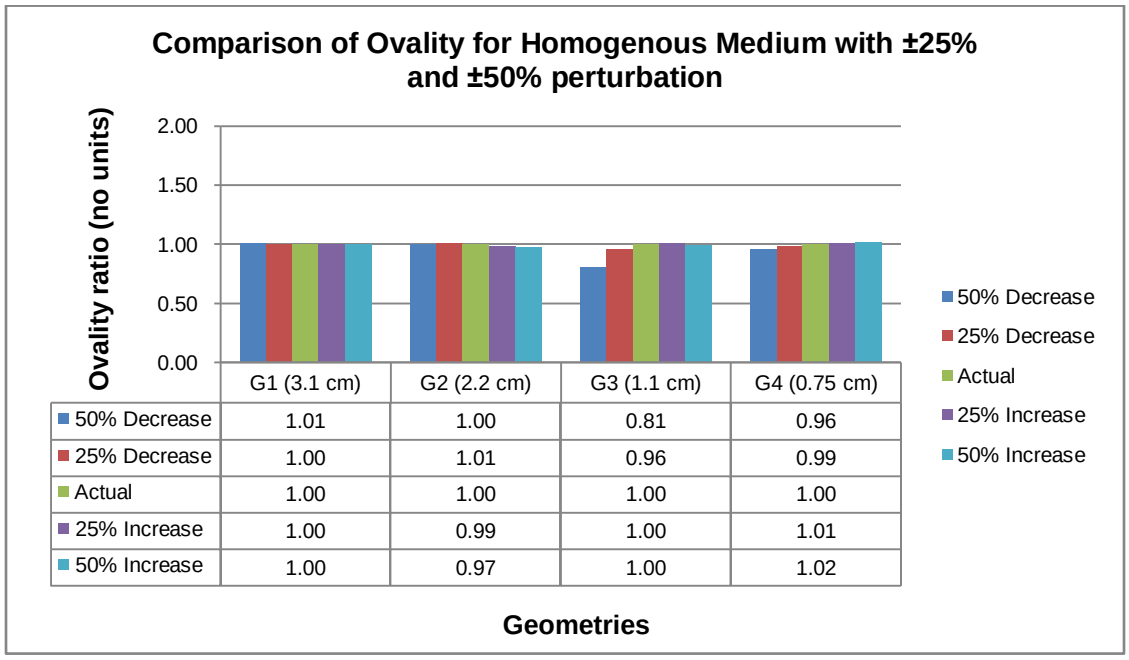

	G1 (3.1 cm)	G2 (2.2 cm)	G3 (1.1 cm)	G4 (0.75 cm)
50% Decrease	1.01	1.00	0.81	0.96
25% Decrease	1.00	1.01	0.96	0.99
Actual	1.00	1.00	1.00	1.00
25% Increase	1.00	0.99	1.00	1.01
50% Increase	1.00	0.97	1.00	1.02

(a)

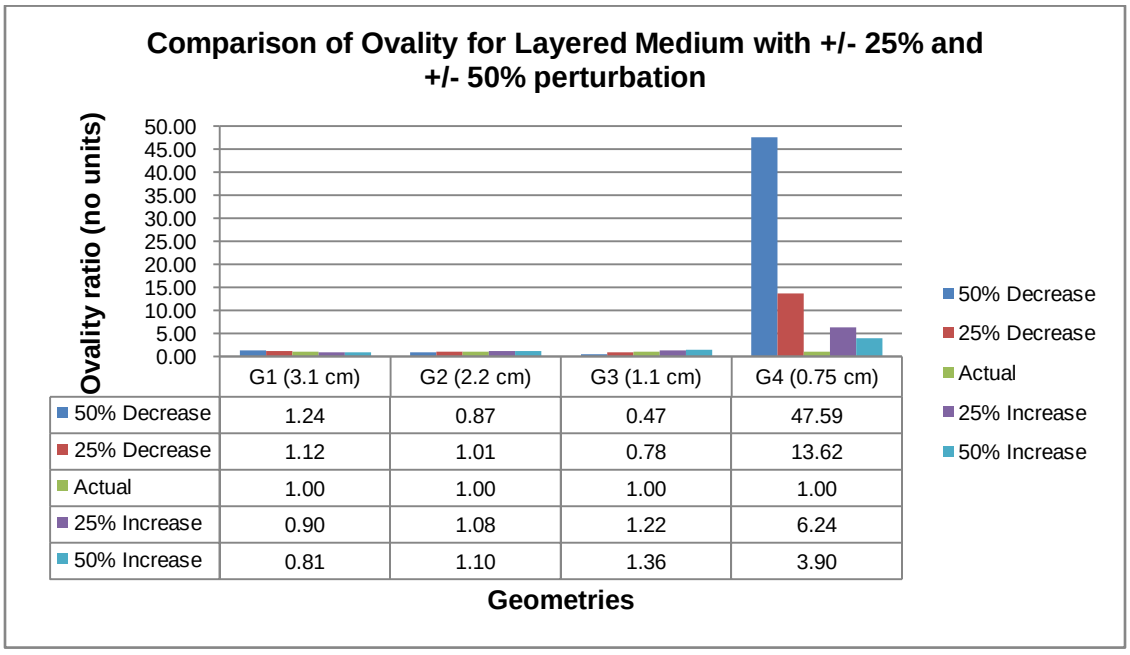

	G1 (3.1 cm)	G2 (2.2 cm)	G3 (1.1 cm)	G4 (0.75 cm)
50% Decrease	1.24	0.87	0.47	47.59
25% Decrease	1.12	1.01	0.78	13.62
Actual	1.00	1.00	1.00	1.00
25% Increase	0.90	1.08	1.22	6.24
50% Increase	0.81	1.10	1.36	3.90

(b)

Figure 3.20 Comparisons of Ovality Ratios across Four Optode Geometries for Anomaly 3 (a) Homogenous Medium, (b) Layered Medium

Table 3.5 Summary of Ovality for G-3 and G-4 under Different Perturbation Conditions

Geometry	%Perturbation	Ovality (no unit)	Baseline (no unit)	Ratio (no unit)
G-3	50% Decrease	3.70E-02	7.94E-02	0.47
	25% Decrease	6.19E-02	7.94E-02	0.78
	Baseline	7.94E-02	7.94E-02	1
	25% Increase	9.66E-02	7.94E-02	1.22
	50% Increase	1.08E-01	7.94E-02	1.36
G-4	50% Decrease	5.78E-03	2.25E-02	1.00
	25% Decrease	3.61E-02	2.25E-02	6.24
	Baseline	2.25E-02	2.25E-02	3.90
	25% Increase	7.87E-02	2.25E-02	13.62
	50% Increase	2.75E-01	2.25E-02	47.59

CHAPTER 4

CONCLUSIONS AND FUTURE WORK

The aim of this study was 1) to assess the effect of S-D geometry on the spatial resolution and localization of isolated absorbers in simulated fNIRS images when using a homogeneous versus a layered geometry for the head tissue background,2) to study what would be the effect of assuming the wrong background tissue optical properties during the image reconstruction process on the spatial resolution and localization of an isolated absorber, both for homogenous and layered tissue geometry backgrounds. The size of the isolated absorber was set to 5 x 5 mm, which was smaller than the known spatial resolution of fNIRS that is in the ~1.5 cm range [27]. The physical size and asymmetries in the reconstructed activation area for three absorber locations (Anomaly 1-3), representing different scenarios in terms of S-D sampling availability, were quantified by area ratio, localization error, FWHM and ovality metrics.

Simulation results showed that for sparse S-D geometries, especially G1, there were significant distortions in reconstructed images when the absorber was located near the edge of the FOV, or right underneath a detector. However, with increasing S-D sampling density these distortions were reduced significantly. Nevertheless there was no improvement in the size of the reconstructed region when sampling with an S-D density beyond 1.1 cm. In fact, image metrics for the 0.75 cm S-D distance geometry became somewhat worse as there was more noise being incorporated into the image reconstruction by the large number of S-D pairs not sampling the activation region. Thus, the hypothesis 2 that spatial resolution increases with increasing S-D density can be accepted, but up to a limit of ~1 cm in S-D separation. For the baseline optical property values used in this work image reconstruction results were qualitatively similar for both the homogeneous and layered tissue geometries and so hypothesis 1 is

rejected. As it is not possible to know the exact tissue optical properties for each subject's head, the effect of assuming the wrong background tissue optical properties on the resulting reconstructed images was assessed for the homogeneous and layered tissue geometries. It was found that both tissue geometries were surprisingly robust to large deviations of μ_s' up to 50%, which largely encompasses the known physiological variation of head tissue optical properties reported in the literatures [24, 32, and 33].The image metrics quantified in this work changed only by a few percent in both the homogenous and layered medium cases and thus these changes are likely to be not significant. This is because changes in μ_s' (and μ_a, as reported in prior work [32]) very nearly acted only as linear multipliers to the A-matrix values and therefore the amplitude, but not the spatial profile of the sensitivity function that affects spatial resolution, changed. Therefore, hypothesis 3, stating that the assumed background optical properties affect the spatial resolution, can be refuted. These findings need to be validated in future simulation work that takes into account the hemodynamic fluctuations [35] and detector noise in the signal generation process. Importantly, future work on fNIRS image modeling that takes into account the geometry of cortical folds and the head's curvature on the resulting two-dimensional and three-dimensional reconstructed images is needed to improve the localization of activation regions, which would be useful for the clinical interpretation of activation maps. Some work along those lines, based on segmented MRI images of a subject's head has already been performed [26-28, 33].

APPENDIX A

CODE FOR DIFFUSION SOLUTION AND IMAGE RECONSTRUCTIONOF HOMOGENOUS AND LAYERED MEDIUM

CODE FOR DIFFUSION SOLUTION OF HOMOGENOUS MEDIUM

```
%%This code computes the A-matrix using the diffusion equation
solution
clearall
clc
Musp=11.1;  %Optical property of the tissue considered
Mua=0.186;

% The Source Matrix
SrcPos = [ 1 1 0
             2.1 1 0
             3.2 1 0
             4.3 1 0
             5.4 1 0
             1 2.1 0
             2.1 2.1 0
             3.2 2.1 0
             4.3 2.1 0
             5.4 2.1 0
             1 3.2 0
             2.1 3.2 0
             3.2 3.2 0
             4.3 3.2 0
             5.4 3.2 0
             1 4.3 0
             2.1 4.3 0
             3.2 4.3 0
             4.3 4.3 0
             5.4 4.3 0
             1 5.4 0
             2.1 5.4 0
             3.2 5.4 0
             4.3 5.4 0
             5.4 5.4 0

          ];
% The Detector Matrix
DetPos = [ 1 1 0
             2.1 1 0
             3.2 1 0
             4.3 1 0
             5.4 1 0
             1 2.1 0
             2.1 2.1 0
             3.2 2.1 0
             4.3 2.1 0
             5.4 2.1 0
             1 3.2 0
             2.1 3.2 0
             3.2 3.2 0
             4.3 3.2 0
```

```
            5.4 3.2 0
            1 4.3 0
            2.1 4.3 0
            3.2 4.3 0
            4.3 4.3 0
            5.4 4.3 0
            1 5.4 0
            2.1 5.4 0
            3.2 5.4 0
            4.3 5.4 0
            5.4 5.4 0  ];
Det_Size = size(DetPos);
% Source- Detector combinations
SD = [ 1 2 1
       1 3 1
       1 6 1
       1 7 1
       1 8 1
       1 11 1
       1 12 1
       1 13 1
       2 1 1
       2 3 1
       2 4 1
       2 6 1
       2 7 1
       2 8 1
       2 9 1
       2 11 1
       2 12 1
       2 13 1
       2 14 1
       3 1 1
       3 2 1
       3 4 1
       3 5 1
       3 6 1
       3 7 1
       3 8 1
       3 9 1
       3 10 1
       3 11 1
       3 12 1
       3 13 1
       3 14 1
       3 15 1
       4 2 1
       4 3 1
       4 5 1
       4 7 1
       4 8 1
       4 9 1
       4 10 1
```

```
4 12 1
4 13 1
4 14 1
4 15 1
5 3 1
5 4 1
5 8 1
5 9 1
5 10 1
5 13 1
5 14 1
5 15 1
6 1 1
6 2 1
6 3 1
6 7 1
6 8 1
6 11 1
6 12 1
6 13 1
6 16 1
6 17 1
6 18 1
7 1 1
7 2 1
7 3 1
7 4 1
7 6 1
7 8 1
7 9 1
7 11 1
7 12 1
7 13 1
7 14 1
7 16 1
7 17 1
7 18 1
7 19 1
8 1 1
8 2 1
8 3 1
8 4 1
8 5 1
8 6 1
8 7 1
8 9 1
8 10 1
8 11 1
8 12 1
8 13 1
8 14 1
8 15 1
8 16 1
```

```
8 17 1
8 18 1
8 19 1
8 20 1
9 2 1
9 3 1
9 4 1
9 5 1
9 7 1
9 8 1
9 10 1
9 12 1
9 13 1
9 14 1
9 15 1
9 17 1
9 18 1
9 19 1
9 20 1
10 3 1
10 4 1
10 5 1
10 8 1
10 9 1
10 13 1
10 14 1
10 15 1
10 18 1
10 19 1
10 20 1
11 1 1
11 2 1
11 3 1
11 6 1
11 7 1
11 8 1
11 12 1
11 13 1
11 16 1
11 17 1
11 18 1
11 21 1
11 22 1
11 23 1
12 1 1
12 2 1
12 3 1
12 4 1
12 6 1
12 7 1
12 8 1
12 9 1
12 11 1
```

```
12 13 1
12 14 1
12 16 1
12 17 1
12 18 1
12 19 1
12 21 1
12 22 1
12 23 1
12 24 1
13 1 1
13 2 1
13 3 1
13 4 1
13 5 1
13 6 1
13 7 1
13 8 1
13 9 1
13 10 1
13 11 1
13 12 1
13 14 1
13 15 1
13 16 1
13 17 1
13 18 1
13 19 1
13 20 1
13 21 1
13 22 1
13 23 1
13 24 1
13 25 1
14 2 1
14 3 1
14 4 1
14 5 1
14 7 1
14 8 1
14 9 1
14 10 1
14 12 1
14 13 1
14 15 1
14 17 1
14 18 1
14 19 1
14 20 1
14 22 1
14 23 1
14 24 1
14 25 1
```

```
15 3 1
15 4 1
15 5 1
15 8 1
15 9 1
15 10 1
15 13 1
15 14 1
15 18 1
15 19 1
15 20 1
15 23 1
15 24 1
15 25 1
16 6 1
16 7 1
16 8 1
16 11 1
16 12 1
16 13 1
16 17 1
16 18 1
16 21 1
16 22 1
16 23 1
17 6 1
17 7 1
17 8 1
17 9 1
17 11 1
17 12 1
17 13 1
17 14 1
17 16 1
17 18 1
17 19 1
17 21 1
17 22 1
17 23 1
17 24 1
18 6 1
18 7 1
18 8 1
18 9 1
18 10 1
18 11 1
18 12 1
18 13 1
18 14 1
18 15 1
18 16 1
18 17 1
18 19 1
```

```
18 20 1
18 21 1
18 22 1
18 23 1
18 24 1
18 25 1
19 7 1
19 8 1
19 9 1
19 10 1
19 12 1
19 13 1
19 14 1
19 15 1
19 17 1
19 18 1
19 20 1
19 22 1
19 23 1
19 24 1
19 25 1
20 8 1
20 9 1
20 10 1
20 13 1
20 14 1
20 15 1
20 18 1
20 19 1
20 23 1
20 24 1
20 25 1
21 11 1
21 12 1
21 13 1
21 16 1
21 17 1
21 18 1
21 22 1
21 23 1
22 11 1
22 12 1
22 13 1
22 14 1
22 16 1
22 17 1
22 18 1
22 19 1
22 21 1
22 23 1
22 24 1
23 11 1
23 12 1
```

```
        23 13 1
        23 14 1
        23 15 1
        23 16 1
        23 17 1
        23 18 1
        23 19 1
        23 20 1
        23 21 1
        23 22 1
        23 24 1
        23 25 1
        24 12 1
        24 13 1
        24 14 1
        24 15 1
        24 17 1
        24 18 1
        24 19 1
        24 20 1
        24 22 1
        24 23 1
        24 25 1
        25 13 1
        25 14 1
        25 15 1
        25 18 1
        25 19 1
        25 20 1
        25 23 1
        25 24 1
        ];

SD_Size = size(SD) ;

V = 2.1898e+10; %velocity of light
Reff = 0.4684;
zBnd = 2/3 * (1+Reff)/(1-Reff)/Musp;
D = V./(3*Musp);
K = 1.7321;
Thickness = 15;
step_x=0.1; %step size (here 1mm step size is considered)
step_y=0.1;
dy = [0.01:step_y:8]; %Voxels in y direction
dx = [0.01:step_x:8];%Voxels in x direction
dz=1;
size(dx);
volVoxel = step_y * step_x * 1;
[x y z]=meshgrid(dx,dy,dz);
x = x(:);
y = y(:);
z = z(:);
nPts = length(x);
```

```
Vox = [x y z];
nMeas = size(SD,1); % Number of measurements

% Looping over each SD Pair
forimeas = 1:length(SD)
iSrc = SD(imeas, 1);  % Actual index
iDet = SD(imeas, 2);
iFrq = SD(imeas, 3);

Src = SrcPos(iSrc,:); % Row indicated with all the coloumns
Det = DetPos(iDet,:);

dmus = D/V;
dmua = -1;

% Move Source and Detector one scattering length into the medium.

Src(3) = Src(3) + 1/Musp;
Det(3) = Det(3) + 1/Musp;
Img = Src;

if (Thickness > 0)
Img(3) = getImageCharge(Src(3), -zBnd);
else
Img(3) = getImageCharge(Src(3),  zBnd);
end

%%  Rescale using amplitude factors from SD structure

PhiSrc = FD_GF(Src, Det, D, K, V);
PhiImg = FD_GF(Img, Det, D, K, V);

% Convert from photon density (J/cm^3) to fluence (W/cm^2) too

Phi0(imeas) = V * (PhiSrc - PhiImg);
Phi0(imeas) = Phi0(imeas) * 1 * 1 ;
phiSa = slabA(Src, Vox, D, K, V, Thickness, zBnd);
phiDa = slabA(Det, Vox, D, K, V, Thickness, zBnd);

% A Matrix Calculation

Atmp(1 : nPts, 1) = phiSa .* (phiDa) .* dmua;
A(imeas, :) = volVoxel * 1* 1 * Atmp.' ;

end
% %
B = -A;
fid= fopen('amat_homo_25src_50decrease.bin','wb');
B=B./ (Phi0' * ones(1,size(B,2)));
fwrite(fid,B,'double');
fclose(fid);
```

CODE FOR IMAGE RECONSTRUCTION OF HOMOGENOOUS AND LAYERED MEDIUM

```
%%The code is written for image reconstruction
clearall;
clc;
det=336;
total_vox=6400;

% load dynot_amat_homo_9srcdet.mat
fid = fopen('amat_homogenous_25src.bin','r');
% fid = fopen('amat_homo_25src_25increase.bin','r');
A= fread(fid, 'double');
A= reshape(A,det, total_vox);
[p,s]=size(A);
for h=1:1:p
Atemp = reshape(A(h,:), 80, 80);
SizeAtemp = size(Atemp);
    Atemp2 = resizing(Atemp);
size(Atemp);
    Atemp3 = resizing(Atemp2');
    m=size(Atemp3);
    Atemp4 = reshape(Atemp3',1,1600);
if h==1
A_new= Atemp4;
else
A_new = [A_new;Atemp4];
end
end
A= A_new;
aftrsize=size(A);
A = [A zeros(size(A)); zeros(size(A)) A];
Size_A = size(A);
loadod_abs3.mat% load Y-matrix
Y=[deltaOD; deltaOD];
size(Y)

a =0.5;
AtA = A'*A;
I = eye(size(A,1),size(A,1));
C = a* max(diag(AtA))*I;
R= eye( size(A,2), size(A,2));
B = A* ( R*A');
foo = R*A'*inv(B+C);

% %Back Projection
Ainv = full(foo);
Img = Ainv*Y;
% %%%%%%%%%%%%%%% L Curve %%%%%%%%%%%%%%%%%%%%%%%%%%%%
% YRecon =A*Img;
% Error = (YRecon-Y);
% ModX = normest(Img);
```

```
% ModErr = normest(Error);
% ModY = normest(Y);
% RelErr = (ModX)/(ModErr);
% %GCV = (ModErr^2)/((trace(I-K*K'))^2)
% size(Error);
Image =Img;
Img_Size = size(Img);
cleardydx;
dy =0.1:0.2:8;
dx =0.1:0.2:8;
dz=1;
  Image2 = reshape( Image, [length(dy) length(dx) length(dz) 2
size(Image,2)] );
Image2=permute(Image2,[1 2 3 5 4]);
  l1min = min(min(min( min(Image2(:,:,:,:,1)) )));
  l2min = min(min(min( min(Image2(:,:,:,:,2)) )));
  l1max = max(max(max( max(Image2(:,:,:,:,1)) )));
  l2max = max(max(max( max(Image2(:,:,:,:,2)) )));
lmin = min([l1min l2min]);
lmax = max([l1max l2max]);
lmin = min([lmin -lmax]);
lmax = max([lmax -lmin]);
  Image3=mean(Image2(:,:,1,:,1),4);
figure,imagesc( dx,dy, Image3, [lminlmax] );
gridon
xlabel('Xaxis (cm)');
ylabel('Yaxis (cm)');
title('Geometry 3');
 [act, no, dact]= kMeansCluster(Image3);
Binaryimg=Image3>max(no);
Actimg=Binaryimg.*Image3;
figure, imagesc(dx, dy,Actimg,[lminlmax] )
gridon
figure, imagesc(Actimg)
gridon
```

CODE FOR DIFFUSION SOLUTION IN LAYERED MEDIUM

```
%%%%%%%%%%%%%%%%%%%%%%%%%%%%%%%%%%%%%%%%%%%%%%%%%%%%%%%%%%%%%%%%%%%%%%%%%%%%%%%%
%%%%%
%This code calculates the A-matrix for a 4-layered medium using the
%executablefile written by Alwin
%%%%%%%%%%%%%%%%%%%%%%%%%%%%%%%%%%%%%%%%%%%%%%%%%%%%%%%%%%%%%%%%%%%%%%%%%%%%%%%%
%%%%%
%
%Date: Oct, 2010
%
%%%%%%%%%%%%%%%%%%%%%%%%%%%%%%%%%%%%%%%%%%%%%%%%%%%%%%%%%%%%%%%%%%%%%%%%%%%%%%%%
%%%%%
%All lengths are in mm
%
%Define variables:
% volx     - length in x direction (in mm)
% voly     - length in y direction (in mm)
% xs,ys    - Co-ordinates of the source
% xd,yd    - Co-ordinates of the detector
% rhos     - distance from source
% rhod     - distance from detector
% clear all;
closeall;
clc;
tic;
volx=60;
voly=60;
amatrix(1,1)=0;
SrcPos = [ 30 30 0
           ];

DetPos = [ 10 10 0
           50 10 0
           10 50 0
           50 50 0
           ];

Det_Size = size(DetPos);

SD=[  1 1 1
        1 2 1
        1 3 1
        1 4 1
   ];

SD_Size = size(SD);
row=length(SD);
A=zeros(row, volx*voly);
%For looping through all the source detector pairs
forimeas = 1:length(SD)
```

```
iSrc = SD(imeas, 1);
iDet = SD(imeas, 2);
xs = SrcPos(iSrc,1);
ys = SrcPos(iSrc,2);
xd = DetPos(iDet,1);
yd = DetPos(iDet,2);

%Distance calulation
n=1;
m=1;
for x=0.5:1:volx
    m=1;
for y=0.5:1:voly
rhos=sqrt((x-xs)^2+(y-ys)^2);
data1=calculation_s(rhos);
rhod=sqrt((x-xd)^2+(y-yd)^2);
data2=calculation_d(rhod);
f1=cell2mat(data1);
f2=cell2mat(data2);
fluence=f1*f2;
amatrix(m,n)=fluence;
m=m+1;
end
n=n+1;
end
%
total_voxels=volx*voly;
Atmp=reshape(amatrix,1,total_voxels);
A(imeas,:) =Atmp;
end
save('cw5_amat.mat', 'A');
toc;
```

APPENDIX B

CODE FOR CALCULATING THE IMAGE METRICS

CODE FOR AREA MEASUREMENT

```
%The purpose of this code was to compute the area of the given
threshold
%image
X=Actimg;%Threashold image
cnt=0;
[row, column]=size(X);
%To count the active pixels in the image
for j=1: column
for i=1:row
if  X(i,j)~= 0
cnt=cnt+1;
end
end
end
cnt;
area=cnt*0.2
```

CODE FOR CENTER OF MASS CALCULATION

```
%%The purpose of this code was to calculate the center in the
%%thresholdimage
% Center of mass (X)=(m1x1+m2x2+...mnxn)/(m1+m2+..mn), where m=value
of
% pixel, x is the x value of (x,y) of pixel
% Center of mass (Y)=(m1y1+m2y2+...mnyn)/(m1+m2+..mn), where m=value
of
% pixel, y is the y value of (x,y) of pixel
%
xref=0;
yref=0;
% calculation in X and Y directions
[row, column]=size(Actimg);
Mass=Actimg;
Xmatrix=zeros(size(Actimg));
Ymatrix=zeros(size(Actimg));
for i=1:row
for j=1:column
if Mass(i,j)~=0
xvalue=abs(xref-j);
yvalue=abs(yref-i);
Xmatrix(i,j)=xvalue;
Ymatrix(i,j)=yvalue;
end
end
end

Xdir=Xmatrix.*Mass;
Ydir=Ymatrix.*Mass;
Tot=sum(sum(Mass));
% To get the output in cm
XX2=((sum(sum(Xdir)))/Tot)/5
YY2=((sum(sum(Ydir)))/Tot)/5
```

CODE FOR 2-D GAUSSIAN FIT

```
%The purpose of this code was to do a 2-D Gaussian fit the image and
obtain
%the major and minor axis of the ellipse.
params0=[max(Image3(:)) 2 2 3 19 19]; % Initial parameters
(Amplitude,a,b,c,x,y)
[px,py] = meshgrid(1:40, 1:40);
%initial paramaters
options = optimset('TolFun',1e-30,'TolX',1e-
30,'MaxFunEvals',Inf,'MaxIter',1000);
[params, resnorm, residual] = lsqnonlin(@objfun,
params0,[],[],options);
op=params(1).*exp(-((params(2).*((px-
params(5)).^2))+(2*params(3).*(py-params(6)).*(px-
params(5)))+(params(4).*((py-params(6)).^2)))); %ellipicalgaussian
figure,mesh(op);
figure,imagesc(op);
a=params(2)
b=params(4)

functionresids = objfun(params)
[D1y, D1x] = size(Image3);
[px,py] = meshgrid(1:D1x, 1:D1y);
pred=params(1).*exp(-((params(2).*((px-
params(5)).^2))+(2*params(3).*(py-params(6)).*(px-
params(5)))+(params(4).*((py-params(6)).^2))));
resids = Image3- pred ;
```

REFERENCES

[1] G. Strangman, D. A. Boas, and J. P. Sutton, "Non-invasive neuroimaging using near-infrared light," *Biol Psychiatry,* vol. 52, pp. 679-93, Oct 1 2002.

[2] H. Liu, D. A. Boas, Y. Zhang, A. G. Yodh, and B. Chance, "Determination of optical properties and blood oxygenation in tissue using continuous NIR light," *Phys Med Biol,* vol. 40, pp. 1983-93, Nov 1995.

[3] J. C. Hebden, "Advances in optical imaging of the newborn infant brain," *Psychophysiology,* vol. 40, pp. 501-10, Jul 2003.

[4] P. Zaramella, F. Freato, A. Amigoni, S. Salvadori, P. Marangoni, A. Suppjei, B. Schiavo, and L. Chiandetti, "Brain auditory activation measured by near-infrared spectroscopy (NIRS) in neonates," *Pediatr Res,* vol. 49, pp. 213-9, Feb 2001.

[5] D. A. Boas, A. M. Dale, and M. A. Franceschini, "Diffuse optical imaging of brain activation: approaches to optimizing image sensitivity, resolution, and accuracy," *Neuroimage,* vol. 23 Suppl 1, pp. S275-88, 2004.

[6] R.Frostig, In vivo optical imaging of brain function. CRC Press, 2002

[7] D. K. Joseph, T. J. Huppert, M. A. Franceschini, and D. A. Boas, "Diffuse optical tomography system to image brain activation with improved spatial resolution and validation with functional magnetic resonance imaging," *Appl Opt,* vol. 45, pp. 8142-51, Nov 1 2006.

[8] A. P. Gibson, J. C. Hebden, and S. R. Arridge, "Recent advances in diffuse optical imaging," *Phys Med Biol,* vol. 50, pp. R1-43, Feb 21 2005

[9] Y. Yamashita, A. Maki, and H. Koizumi, "Wavelength dependence of the precision of noninvasive optical measurement of oxy-, deoxy-, and total-hemoglobin concentration," *Med Phys,* vol. 28, pp. 1108-14, Jun 2001.

[10] G. Strangman, M. A. Franceschini, and D. A. Boas, "Factors affecting the accuracy of near-infrared spectroscopy concentration calculations for focal changes in oxygenation parameters," *Neuroimage,* vol. 18, pp. 865-79, Apr 2003.

[11] H. Obrig and A. Villringer, "Beyond the visible--imaging the human brain with light," *J Cereb Blood Flow Metab,* vol. 23, pp. 1-18, Jan 2003.

[12] A. Bozkurt and B. Onaral, "Safety assessment of near infrared light emitting diodes for diffuse optical measurements," *Biomed Eng Online,* vol. 3, p. 9, Mar 22 2004.

[13] T. Tarvainen, M. Vauhkonen, V. Kolehmainen, S. R. Arridge, and J. P. Kaipio, "Coupled radiative transfer equation and diffusion approximation model for photon migration in turbid medium with low-scattering and non-scattering regions," *Phys Med Biol,* vol. 50, pp. 4913-30, Oct 21 2005.

[14] S. R. Arridge and J. C. Hebden, "Optical imaging in medicine: II. Modelling and reconstruction," *Phys Med Biol,* vol. 42, pp. 841-53, May 1997.

[15] R. C. Haskell, L. O. Svaasand, T. T. Tsay, T. C. Feng, M. S. McAdams, and B. J. Tromberg, "Boundary conditions for the diffusion equation in radiative transfer," *J Opt Soc Am A Opt Image Sci Vis,* vol. 11, pp. 2727-41, Oct 1994.

[16] A. Kienle and M. S. Patterson, "Improved solutions of the steady-state and the time-resolved diffusion equations for reflectance from a semi-infinite turbid medium," *J Opt Soc Am A Opt Image Sci Vis,* vol. 14, pp. 246-54, Jan 1997.

[17] T. J. Huppert, S. G. Diamond, M. A. Franceschini, and D. A. Boas, "HomER: a review of time-series analysis methods for near-infrared spectroscopy of the brain," *Appl Opt,* vol. 48, pp. D280-98, Apr 1 2009. T. J. Huppert, S. G. Diamond, M. A. Franceschini, and D. A. Boas, "HomER: a review of time-series analysis methods for near-infrared spectroscopy of the brain," *Appl Opt,* vol. 48, pp. D280-98, Apr 1 2009.

[18] A. Kienle, M. S. Patterson, N. Dognitz, R. Bays, G. Wagninures, and H. van den Bergh, "Noninvasive Determination of the Optical Properties of Two-Layered Turbid Media," *Appl Opt,* vol. 37, pp. 779-791, Feb 1 1998.

[19] A. Liemert and A. Kienle, "Light diffusion in N-layered turbid media: steady-state domain," *J Biomed Opt,* vol. 15, p. 025003, Mar-Apr 2010.

[20] D. Boas, J. Culver, J. Stott, and A. Dunn, "Three dimensional Monte Carlo code for photon migration through complex heterogeneous media including the adult human head," *Opt Express,* vol. 10, pp. 159-70, Feb 11 2002.

[21] http://omlc.ogi.edu/spectra/hemoglobin/summary.html

[22] HR. Eggert and V. Blazek, “Optical properties of human brain tissue, meninges, and brain tumors in the spectral range of 200 to 900 nm,” *Neurosurgery,* vol. 21, pp. 459-64, Oct 1987

[23] F.H.Netter, The Ciba collection of medical illustrations-Nervous system part 1, Anatomy and physiology. New Jersey: Ciba-Geigy Corporation, 1994.

[24] E. Okada, M. Firbank, M. Schweiger, S. R. Arridge, M. Cope, and D. T. Delpy, "Theoretical and experimental investigation of near-infrared light propagation in a model of the adult head," *Appl Opt,* vol. 36, pp. 21-31, Jan 1 1997.

[25] E. Okada and D. T. Delpy, "Near-infrared light propagation in an adult head model. I. Modeling of low-level scattering in the cerebrospinal fluid layer," *Appl Opt,* vol. 42, pp. 2906-14, Jun 1 2003.

[26] Y. Fukui, Y. Ajichi, and E. Okada, "Monte Carlo prediction of near-infrared light propagation in realistic adult and neonatal head models," *Appl Opt,* vol. 42, pp. 2881-7, Jun 1 2003.

[27] B. R. White and J. P. Culver, "Quantitative evaluation of high-density diffuse optical tomography: in vivo resolution and mapping performance," *J Biomed Opt,* vol. 15, p. 026006, Mar-Apr 2010.

[28] S. P. Koch, C. Habermehl, J. Mehnert, C. H. Schmitz, S. Holtze, A. Villringer, J. Steinbrink, and H. Obrig, "High-resolution optical functional mapping of the human somatosensory cortex," *Front Neuroenergetics,* vol. 2, p. 12, 2010.

[29] B. Khan, F. Tian, K. Behbehani, M. I. Romero, M. R. Delgado, N. J. Clegg, L. Smith, D. Reid, H. Liu, and G. Alexandrakis, "Identification of abnormal motor cortex activation patterns in children with cerebral palsy by functional near-infrared spectroscopy," *J Biomed Opt,* vol. 15, p. 036008, May-Jun 2010.

[30] F. Tian, G. Alexandrakis, and H. Liu, "Optimization of probe geometry for diffuse optical brain imaging based on measurement density and distribution," *Appl Opt,* vol. 48, pp. 2496-504, May 1 2009.

[31] F. Abdelnour, B. Schmidt, and T. J. Huppert, "Topographic localization of brain activation in diffuse optical imaging using spherical wavelets," *Phys Med Biol,* vol. 54, pp. 6383-413, Oct 21 2009.

[32] A. Kanneganti, “Optimization of reconstructed parameters in brain activation studies”, Dec 2008

[33] C.-K. Lee, C.-W.Sun, P.-L.Lee, H.-C.Lee, C. Yang, C.-P.Jiang, Y.-P.Tong, T.-C.Yeh, and J.-C. Hsieh, "Study of photon migration with various source-detector separations in near-infrared spectroscopic brain imaging based on three-dimensional Monte Carlo modeling," *Optics express,* vol. 13, pp. 8339-48, 2005.

[34] T. Li, H. Gong, and Q. Luo, "Visualization of light propagation in visible Chinese human head for functional near-infrared spectroscopy," *J Biomed Opt,* vol. 16, p. 045001, Apr 2011.

[35] G. Strangman, J. P. Culver, J. H. Thompson, and D. A. Boas, "A quantitative comparison of simultaneous BOLD fMRI and NIRS recordings during functional brain activation," Neuroimage, vol. 17, pp. 719-31, Oct 2002.

BIOGRAPHICAL INFORMATION

Niranjana Nandakumar was born in Salem, Tamil Nadu on October 6th, 1986. She received her Bachelor's of Engineering in Biomedical Instrumentation from Avinashilingam Deemed University in 2008. Her interest in research persuaded her to do Master's in Biomedical Engineering at University of Texas at Arlington. She has plans to do her Phd after some years of experience in biomedical industry.